Journal of Computational Physics 415 (2020) 109535

Contents lists available at ScienceDirect

Journal of Computational Physics

www.elsevier.com/locate/jcp

A velocity-space adaptive unified gas kinetic scheme for continuum and rarefied flows

Tianbai Xiao [a], Chang Liu [b], Kun Xu [b,c,d,*], Qingdong Cai [e]

[a] Department of Mathematics and Steinbuch Centre for Computing, Karlsruhe Institute of Technology, Karlsruhe 76131, Germany
[b] Department of Mathematics, Hong Kong University of Science and Technology, Clear Water Bay, Kowloon, Hong Kong
[c] Department of Mechanical and Aerospace Engineering, Hong Kong University of Science and Technology, Clear Water Bay, Kowloon, Hong Kong
[d] Shenzhen Research Institute, Hong Kong University of Science and Technology, Shenzhen 518057, China
[e] Department of Mechanics and Engineering Science, College of Engineering, Peking University, Beijing 100871, China

ARTICLE INFO

Article history:
Received 16 February 2018
Received in revised form 30 January 2020
Accepted 4 May 2020
Available online 19 May 2020

Keywords:
Unified gas kinetic scheme
Gas kinetic scheme
Multiscale flow
Non-equilibrium phenomena
Adaptive velocity space

ABSTRACT

Compressible flow has intrinsically multiple scale nature due to the large variations of gas density and characteristic scale of flow structure, especially in hypersonic and reentry problems. It is challenging to construct an accurate and efficient numerical algorithm to capture non-equilibrium flow physics across different regimes. In this paper, a unified gas kinetic scheme with adaptive velocity space (AUGKS) for multiscale flow transport will be developed. In near-equilibrium flow region, particle distribution function is close to the Chapman-Enskog expansion and can be formulated analytically, where only macroscopic conservative flow variables are updated. With the emergence of non-equilibrium effect, the AUGKS automatically switches to the original unified gas kinetic scheme (UGKS) with a discrete velocity space to follow the evolution of particle distribution function. A criterion is proposed to quantify the non-equilibrium and is used for the switch between continuous and discrete particle velocity space. Following the scale-dependent local evolving solution, the AUGKS presents the discretized gas dynamic equations directly on the cell size and time step scales, i.e., the so-called direct modeling method. As a result, the scheme is able to capture the cross-scale flow physics from particle transport to hydrodynamic wave propagation, and provides a continuous variation of solutions from the Boltzmann to the Euler equations. Different from conventional DSMC-Fluid hybrid method, the AUGKS does not need a buffer zone to match up kinetic and hydrodynamic solutions. Instead, continuous and discrete particle velocity spaces are automatically and robustly switched, such as translating the continuous Chapman-Enskog distribution function to the discrete grid points in the velocity space. Therefore, the AUGKS is feasible for the numerical simulations with unsteadiness and complex geometries. Compared with the asymptotic preserving (AP) method which solves kinetic equation uniformly over entire computational domain with discretized velocity space, the current velocity-space adaptive unified scheme speeds up the computation, reduces the memory requirement significantly, and maintains the equivalent accuracy for multiscale flow simulations. Many test cases validate the current approach. The AUGKS provides an effective tool for non-equilibrium flow studies.

* Corresponding author at: Department of Mathematics, Hong Kong University of Science and Technology, Clear Water Bay, Kowloon, Hong Kong.
E-mail addresses: tianbaixiao@gmail.com (T. Xiao), maliu@ust.hk (C. Liu), makxu@ust.hk (K. Xu), caiqd@pku.edu.cn (Q. Cai).

https://doi.org/10.1016/j.jcp.2020.109535
0021-9991/

1. Introduction

The gaseous flow shows a diverse set of behaviors on different characteristic scales. For example, within the mean free path and collision time of gas molecules, particles travel freely during most of time with rare intermolecular collisions, leading to peculiar non-equilibrium flow dynamics. Meanwhile, with the enlargement of modeling scale to a macroscopic hydrodynamic level, the accumulating effect of particle collisions results in an equalization of local temperature and velocity, where the moderate non-equilibrium effects can be well described by viscous transport, heat conduction and mass diffusion, i.e., the so called transport phenomena [1]. From microscopic particle transport to macroscopic fluid motion, there is a continuous variation of flow dynamics. Generally, different flow regimes can be categorized qualitatively according to the Knudsen number, which is defined as the ratio of the molecular mean free path to a characteristic physical length scale. With the variation of Kn, the whole flow domain can be divided into continuum ($Kn < 0.001$), slip ($0.001 < Kn < 0.1$), transition ($0.1 < Kn < 10$), and free molecular regimes ($Kn > 10$) [2]. When Kn is large, the particle transport and collision can be depicted separately in the Boltzmann equation. In another limit with extremely small Kn, the Navier-Stokes equations are routinely used to describe macroscopic flow evolution.

The traditional computational fluid dynamics targets to get numerical solutions of the corresponding governing equations. For example, the most widely used numerical methods for the Boltzmann equation are the direct Boltzmann solvers [3] and the direct simulation Monte Carlo (DSMC) method [4]. In the former methodology, a discretized particle velocity space is constructed and the particle distribution function is updated from the transport and collision terms respectively. On the other hand, the DSMC method mimics the same physical process while the distribution function is now represented by a large amount of test particles and the collision term is calculated statistically. Due to the splitting treatment of particle transport and collision, the mesh size and time step should be restricted by the mean free path and collision time, and the computational cost is proportional to the amount of discretized velocity points or test particles used in the simulation. Meanwhile, the compressible Navier-Stokes solvers are mostly based on the Riemann solvers for inviscid flux and the central difference method for viscous terms. The macroscopic flow variables are followed in the simulation. Compared with the kinetic methods, the computational cost of continuum flow solvers is much reduced.

The rapid development of aerospace industry faces new challenges for accurate and efficient simulation of complex flows. For example, when a shuttle re-enters into the atmosphere, the surrounding gas has a large density variation from the rarefied upper atmosphere to lower continuum region, and the flow physics covers all regimes during the landing process. Besides, localized non-equilibrium flow structures emerge around the vehicle in hypersonic cruise as a result of the geometric effect, such as shock, rarefaction wave, boundary layer, and wake turbulence. The local Knudsen number for the flow passing through a hypersonic vehicle in near space flight can cover a wide range of values with five orders of magnitude. It is natural to couple different numerical methods in different regions to calculate aerodynamic force and heat efficiently. Therefore, hybrid algorithms which combine continuum and kinetic approaches become popular to simulate multiple scale flows with the coexistence of continuum and rarefied gas dynamics [5–23]. In these numerical schemes, the main flow structure is simulated by the continuum methods efficiently, where the highly dissipative non-equilibrium region is resolved by the kinetic methods. Due to the complicated fivefold collision integral in the Boltzmann equation, the prevailing kinetic solver used in the hybrid methods is mostly the DSMC method. In the calculation, a dynamic parameter is needed to determine the location to separate different flow regimes. The implementation of parallel computing for the hybrid method is straightforward since the physical domain has already been divided into blocks on different computational nodes.

In kinetic theory, the Chapman-Enskog expansion [24] bridges the Boltzmann and hydrodynamic solutions. Although this successive expansion is mathematically attractive, there is little information provided about the intrinsic scale for the validation of macroscopic equations, such as the use of non-penetrating fluid element in the Navier-Stokes (NS) modeling. The success of the mathematical derivation of high-order equations with inclusion of the so called Burnett or super-Burnett terms seems limited due to the lack of specified modeling scales in these extended hydrodynamic equations. Besides, due to the uncertainty in choosing the length scale in the definition of Knudsen number, it becomes rather tough to predict a universal breakdown criterion for the Chapman-Enskog expansion and the use of the NS solutions, although it is defined empirically that the NS equations are valid when $Kn \leq 0.001$. In addition, on the particle mean free path and collision time scales, the kinetic method has much more degrees of freedom in the description of distribution function, which needs to be shrunken to a few macroscopic variables in the buffer zone with a coarse-grained process, such as density, momentum, energy, stress and heat flux. The inherent incompatibility between the particle-based and PDE-based methods also leads to a considerable difficulty in the hybridization. Usually a buffer zone is constructed delicately for the information exchange between kinetic and continuum solutions, which can hardly be defined accurately in a time-dependent unsteady flow problem.

In recent years, the unified gas kinetic scheme (UGKS) has been developed for multiscale flow simulations [25–29]. Based on the direct modeling on the mesh size scale, a time-evolving flux function based on the kinetic equation provides a smooth transition from particle transport to hydrodynamic wave propagation with the increasing of evolution time. The UGKS is an asymptotic preserving (AP) scheme, which preserves the discrete analogy of the Chapman-Enskog expansion when the time scale in the simulation is much larger than the particle collision time [30]. More specifically, the UGKS has the Euler limit for shock structure computation, with the cell size being much larger than particle mean free path ℓ (physical shock thickness is $O(\ell)$), and it gives the NS limit for boundary layer, where the cell size can be much larger than

particle mean free path as well, but less than boundary layer thickness $O(\sqrt{\ell})$. The success to get the Navier-Stokes limit in UGKS is due to the coupling of particle transport and collision in the construction of evolving particle distribution function at the cell interface, from which the Chapman-Enskog expansion for the NS solutions can be obtained automatically from the integral solution of the kinetic relaxation model in the small Knudsen number limit [27,31]. However, for the UGKS the memory requirement and computational cost due to the discretized velocity space limit its efficient applications. In this paper, we develop an adaptive unified gas kinetic scheme (AUGKS) with dynamically coupled continuous and discrete particle velocity space in a unified framework. In the near-equilibrium region, the Chapman-Enskog expansion is used for the construction of distribution function with a continuous velocity space, and the corresponding discrete distribution function can be easily constructed from the Chapman-Enskog expansion if needed. Thus, in these regions only macroscopic conservative flow variables are stored and updated in the simulation. With the increase of non-equilibrium effects, the AUGKS tracks the evolution of distribution function directly with a discrete velocity space. Based on the Chapman-Enskog expansion, a criterion to switch continuous-discrete velocity space in the simulation is proposed and validated through numerical experiments. Compared with the original UGKS method, the current adaptive scheme frees the memory requirement in the near-equilibrium flow regime and speeds up the computation, but provides the same physical solution. Due to the use of particle distribution function in the whole computational domain, i.e., updated or reconstructed ones in different regions, the AUGKS avoids domain decomposition in the physical space to distinguish and connect fluid and kinetic solvers. In other words, no buffer zone is needed in AUGKS.

This paper is organized as follows. Section 2 is a brief introduction of kinetic theory. Section 3 presents the numerical implementation of the adaptive unified gas kinetic scheme and proposes a switching criterion of the velocity space adaptation. Section 4 includes numerical examples to demonstrate the performance of the current scheme. The last section is the conclusion.

2. Gas kinetic modeling

The gas kinetic theory describes the time-space evolution of particle distribution function $f(\mathbf{x}, \mathbf{u}, t)$, where $\mathbf{x} \in \mathcal{R}^3$ is space variable and $\mathbf{u} \in \mathcal{R}^3$ is particle velocity. In the absence of external force field, the Boltzmann equation of a monatomic dilute gas becomes,

$$f_t + \mathbf{u} \cdot \nabla_{\mathbf{x}} f = Q(f, f) = \int_{\mathcal{R}^3} \int_{\mathcal{S}^2} \left[f(\mathbf{u}') f(\mathbf{u}_1') - f(\mathbf{u}) f(\mathbf{u}_1) \right] \mathcal{B}(\cos\theta, g) d\mathbf{\Omega} d\mathbf{u}_1, \tag{1}$$

where $\mathbf{u}, \mathbf{u_1}$ are the pre-collision velocities of two classes of molecules, and $\mathbf{u}', \mathbf{u_1}'$ are the corresponding post-collision velocities. The collision kernel $\mathcal{B}(\cos\theta, g)$ measures the strength of collisions in different directions, where θ is the deflection angle and $g = |\mathbf{g}| = |\mathbf{u} - \mathbf{u_1}|$ is the magnitude of relative pre-collision velocity. The $\mathbf{\Omega}$ is the unit vector along the relative post-collision velocity $\mathbf{u}' - \mathbf{u_1}'$, and the deflection angle θ satisfies $\cos\theta = \mathbf{\Omega} \cdot \mathbf{g}/g$. The conservation of momentum and energy leads to the following relations,

$$\begin{aligned} \mathbf{u}' &= \frac{\mathbf{u} + \mathbf{u_1}}{2} + \frac{|\mathbf{u} - \mathbf{u_1}|}{2} \mathbf{\Omega} = \mathbf{u} + \frac{g\mathbf{\Omega} - \mathbf{g}}{2}, \\ \mathbf{u_1}' &= \frac{\mathbf{u} + \mathbf{u_1}}{2} - \frac{|\mathbf{u} - \mathbf{u_1}|}{2} \mathbf{\Omega} = \mathbf{u_1} - \frac{g\mathbf{\Omega} - \mathbf{g}}{2}. \end{aligned} \tag{2}$$

Due to the complicated fivefold integration in the Boltzmann collision operator, some simplified kinetic models have been constructed, such as the Shakhov [32]. In this model, the Boltzmann collision operator $Q(f, f)$ is replaced with a relaxation operator $S(f)$, which writes,

$$\begin{aligned} f_t + \mathbf{u} \cdot \nabla_{\mathbf{x}} f &= S(f) = \frac{f^+ - f}{\tau}, \\ f^+ &= \rho \left(\frac{\lambda}{\pi} \right)^{\frac{3}{2}} e^{-\lambda(\mathbf{u}-\mathbf{U})^2} \left[1 + (1 - Pr)\mathbf{c} \cdot \mathbf{q} \left(\frac{\mathbf{c}^2}{RT} - 5 \right) / (5pRT) \right], \end{aligned} \tag{3}$$

where $\tau = \mu/p$ is the collision time. The macroscopic density, velocity, temperature, and heat flux are marked with $\rho, \mathbf{U}, T, \mathbf{q}$. The $\mathbf{c} = \mathbf{u} - \mathbf{U}$ is particle peculiar velocity, Pr is the Prandtl number, R is the gas constant, and $\lambda = \rho/(2p)$. In this paper, the numerical simulations will be conducted by either the full Boltzmann or the Shakhov collision terms.

The macroscopic conservative flow variables are related to the moments of particle distribution function via

$$\mathbf{W} = \begin{pmatrix} \rho \\ \rho \mathbf{U} \\ \rho E \end{pmatrix} = \int f \psi d\mathbf{u},$$

and the collision terms satisfy the compatibility condition,

$$\int Q(f,f)\psi d\mathbf{u} = \int S(f)\psi d\mathbf{u} = 0,$$

where $\psi = \left(1, \mathbf{u}, \frac{1}{2}\mathbf{u}^2\right)^T$ is a vector of collision invariants. Here we rewrite the collision terms $Q(f,f)$ and $S(f)$ into a general form $Q(f)$.

With a local constant collision time τ, the integral solution of Eq. (3) can be constructed along the characteristic line,

$$f(\mathbf{x},t,\mathbf{u}) = \frac{1}{\tau}\int_{t^0}^{t} f^+(\mathbf{x}',t',\mathbf{u})e^{-(t-t')/\tau}dt' + e^{-(t-t^0)/\tau}f_0(\mathbf{x}^0,\mathbf{u}), \tag{4}$$

where $\mathbf{x}' = \mathbf{x} - \mathbf{u}(t-t')$ is the particle trajectory, and f_0 is the distribution function at the initial time $t = t^0$ with $\mathbf{x}^0 = \mathbf{x} - \mathbf{u}(t-t^0)$. Based on the above evolving solution, the corresponding discretized gas dynamic equations on the cell size and time step scales are constructed in the gas kinetic scheme.

3. Adaptive unified gas kinetic scheme

In this section, we will present the principle and numerical implementation of the velocity-space adaptive unified gas kinetic scheme (AUGKS). The original gas kinetic scheme with continuous and discrete particle velocity space will be introduced first. The detailed coupling of continuum and kinetic treatments and the switching criterion for velocity space transformation will be discussed. For simplicity, the following introduction is based on two-dimensional case, while the extension to three dimension is straightforward.

3.1. Unified gas kinetic scheme with discrete velocity space

With the notation of cell averaged quantities in a control volume,

$$\mathbf{W}_{i,j}^n = \frac{1}{\Delta x_i \Delta y_j}\int_{x_{i-1/2}}^{x_{i+1/2}}\int_{y_{j-1/2}}^{y_{j+1/2}} \mathbf{W}(x,y,t^n)dxdy,$$

$$f_{i,j,l,m}^n = \frac{1}{\Delta x_i \Delta y_j \Delta u_l \Delta v_m}\int_{x_{i-1/2}}^{x_{i+1/2}}\int_{y_{j-1/2}}^{y_{j+1/2}}\int_{u_{l-1/2}}^{u_{l+1/2}}\int_{v_{m-1/2}}^{v_{m+1/2}} f(x,y,t^n,u,v)dxdydudv,$$

the updates of macroscopic conservative variables and particle distribution function are coupled in the UGKS,

$$\begin{aligned}\mathbf{W}_{i,j}^{n+1} = \mathbf{W}_{i,j}^n &+ \frac{1}{\Delta x_i \Delta y_j}\int_{t^n}^{t^{n+1}}\int_{y_{j-1/2}}^{y_{j+1/2}} (\mathbf{F}_{i-1/2} - \mathbf{F}_{i+1/2})dydt \\ &+ \frac{1}{\Delta x_i \Delta y_j}\int_{t^n}^{t^{n+1}}\int_{x_{i-1/2}}^{x_{i+1/2}} (\mathbf{F}_{j-1/2} - \mathbf{F}_{j+1/2})dxdt,\end{aligned} \tag{5}$$

$$\begin{aligned}f_{i,j,l,m}^{n+1} = f_{i,j,l,m}^n &+ \frac{1}{\Delta x_i \Delta y_j}\int_{t^n}^{t^{n+1}}\int_{y_{j-1/2}}^{y_{j+1/2}} u_l(f_{i-1/2,j,l,m} - f_{i+1/2,j,l,m})dydt \\ &+ \frac{1}{\Delta x_i \Delta y_j}\int_{t^n}^{t^{n+1}}\int_{x_{i-1/2}}^{x_{i+1/2}} v_m(f_{i,j-1/2,l,m} - f_{i,j+1/2,l,m})dxdt \\ &+ \int_{t^n}^{t^{n+1}} Q(f_{i,j,l,m})dt,\end{aligned} \tag{6}$$

where $\mathbf{F}_{i\pm1/2}$ are the fluxes of conservative variables.

In UGKS, the flux function is evaluated through the time-dependent particle distribution at the cell interface, which is constructed from the evolving solution of the Shakhov equation. With the defined cell interface $x_{i+1/2} = 0$, $y_j = 0$ and initial time $t^n = 0$, at a local constant collision time τ, the integral solution in Eq. (4) can be written as,

$$f(0,0,t,u_l,v_m,\xi) = \frac{1}{\tau}\int_0^t f^+(x',y',t',u_l,v_m,\xi)e^{-(t-t')/\tau}dt' + e^{-t/\tau}f_0(x^0,y^0,u_l,v_m,\xi), \tag{7}$$

where $x' = -u_l(t-t')$ and $y' = -v_m(t-t')$ are the particle trajectories, and x^0, y^0 are the initial locations for the particle which passes through the cell interface at time t. Here f_0 is the particle distribution function at the beginning of n-th time step. The internal degree of freedom ξ describes the random motion in z direction. This scale-dependent evolution solution is used to define the interface distribution function in Eq. (6), which provides the continuous spectrum of flow dynamics from the kinetic non-equilibrium particle transport in the initial distribution function f_0 to the hydrodynamic wave propagation in the integration of equilibrium state f^+. The real flow physics simulated in the scheme depends on the ratio of evolving time t (i.e., the time step in the computation) to the particle collision time τ.

To the second order accuracy, the initial particle distribution function f_0 is reconstructed as

$$f_0(x,y,u_l,v_m,\xi) = \begin{cases} f^L_{i+1/2,j,l,m} + \sigma_{i,j,l,m}x + \theta_{i,j,l,m}y, & x \le 0, \\ f^R_{i+1/2,j,l,m} + \sigma_{i+1,j,l,m}x + \theta_{i+1,j,l,m}y, & x > 0, \end{cases} \tag{8}$$

where $(f^L_{i+1/2,j,l,m}, f^R_{i+1/2,j,l,m})$ are the reconstructed initial distribution functions at the left and right hand sides of a cell interface, and (σ, θ) are the corresponding slopes along x and y directions. In addition, the equilibrium distribution function around a cell interface is constructed as

$$f^+ = f_0^+\left[1 + (1-H[x])\bar{a}^L x + H[x]\bar{a}^R x + \bar{b}y + \bar{A}t\right] = f_0^+\left(1 + \bar{a}^{L,R}x + \bar{b}y + \bar{A}t\right), \tag{9}$$

where f_0^+ is the equilibrium distribution at $(x=0, y=0, t=0)$, and $H[x]$ is the Heaviside step function. The coefficients $(\bar{a}^{L,R}, \bar{b}, \bar{A})$ are the spatial and temporal derivatives of the equilibrium distribution function, which can be expanded as,

$$\begin{aligned} \bar{a}^{L,R} &= \bar{a}_1^{L,R} + \bar{a}_2^{L,R}u + \bar{a}_3^{L,R}v + \bar{a}_4^{L,R}\frac{1}{2}(u^2+v^2+\xi^2) = \bar{a}_\alpha^{L,R}\psi_\alpha, \\ \bar{b} &= \bar{b}_1 + \bar{b}_2 u + \bar{b}_3 v + \bar{b}_4\frac{1}{2}(u^2+v^2+\xi^2) = \bar{b}_\alpha\psi_\alpha, \\ \bar{A} &= \bar{A}_1 + \bar{A}_2 u + \bar{A}_3 v + \bar{A}_4\frac{1}{2}(u^2+v^2+\xi^2) = \bar{A}_\alpha\psi_\alpha. \end{aligned}$$

The equilibrium distribution function f_0^+ at the cell interface depends on the local macroscopic flow variables $\mathbf{W}_0$. Based on the compatibility condition,

$$\int (f^+ - f)|_{x=0,t=0}\psi du dv d\xi = 0,$$

we get

$$\int f_0^+\psi_\alpha du dv d\xi = \mathbf{W}_0 = \sum_{u_l>0} f^L_{i+1/2,j,l,m}\psi du dv d\xi + \sum_{u_l<0} f^R_{i+1/2,j,l,m}\psi du dv d\xi.$$

After the determination of the equilibrium state at the cell interface, its spatial derivatives $\bar{a}^L, \bar{a}^R$ can be obtained from the slopes of conservative flow variables on both sides of a cell interface,

$$\begin{aligned} \left(\frac{\partial \mathbf{W}}{\partial x}\right)^L &\simeq \frac{\mathbf{W}_0 - \mathbf{W}_i}{\Delta x^-} = \int \bar{a}^L f_0^+\psi du dv d\xi = \bar{M}^0_{\alpha\beta}\bar{a}^L_\beta, \\ \left(\frac{\partial \mathbf{W}}{\partial x}\right)^R &\simeq \frac{\mathbf{W}_{i+1} - \mathbf{W}_0}{\Delta x^+} = \int \bar{a}^R f_0^+\psi du dv d\xi = \bar{M}^0_{\alpha\beta}\bar{a}^R_\beta, \end{aligned}$$

where $\bar{M}^0_{\alpha\beta} = \int f_0^+\psi_\alpha\psi_\beta du dv d\xi$ is a known matrix, $\bar{\mathbf{a}}^{L,R} = (\bar{a}_1^{L,R}, \bar{a}_2^{L,R}, \bar{a}_3^{L,R}, \bar{a}_4^{L,R})^T$. Here $\Delta x^+ = x_{i+1} - x_{i+1/2}$ and $\Delta x^- = x_{i+1/2} - x_i$ are the distances from the cell interface to cell centers. The tangential derivative $\bar{b}$ is obtained from

$$\int \bar{b}\psi f_0^+ du dv d\xi = \sum_{l,m}(\theta_{i,j,l,m}H[u_l] + \theta_{i+1,j,l,m}(1-H[u_l]))\psi.$$

The time derivative $\bar{A}$ is related to the temporal variation of conservative flow variables,

$$\frac{\partial \mathbf{W}}{\partial t} = \int \bar{A} f_0^+\psi du dv d\xi,$$

and it can be calculated via the time derivative of the compatibility condition

$$\frac{d}{dt}\int (f^+ - f)\psi du dv d\xi \mid_{x=0,t=0} = 0.$$

With the help of the Euler equations, it gives

$$-\int u\frac{\partial f^+}{\partial x}\psi du dv d\xi - \int v\frac{\partial f^+}{\partial y}\psi du dv d\xi = \frac{\partial \mathbf{W}}{\partial t} = \int \bar{A} f_0^+ \psi du dv d\xi,$$

and the spatial derivatives in the above equation have been obtained from the initial equilibrium reconstruction in Eq. (9). Therefore, we have

$$\int \bar{A} f_0^+ \psi du dv d\xi = -\int (\bar{a}^{L,R} u + \bar{b} v) f_0^+ \psi du dv d\xi,$$

from which $\bar{A} = (\bar{A}_1, \bar{A}_2, \bar{A}_3, \bar{A}_4)^T$ are fully determined.

After all coefficients are obtained, the time dependent interface distribution function becomes

$$\begin{aligned} f(0,0,t,u_l,v_m,\xi) =& \left(1 - e^{-t/\tau}\right) f_0^+ \\ &+ \left(\tau(-1 + e^{-t/\tau}) + te^{-t/\tau}\right)\bar{a}^{L,R} u_l f_0^+ \\ &+ \left(\tau(-1 + e^{-t/\tau}) + te^{-t/\tau}\right)\bar{b} v_m f_0^+ \\ &+ \tau\left(t/\tau - 1 + e^{-t/\tau}\right)\bar{A} f_0^+ \\ &+ e^{-t/\tau}\left[\left(f^L_{i+1/2,j,l,m} - u_l t\sigma_{i,j,l,m} - v_m t\theta_{i,j,l,m}\right) H[u_l]\right. \\ &\left. + \left(f^R_{i+1/2,j,l,m} - u_l t\sigma_{i+1,j,l,m} - v_m t\theta_{i+1,j,l,m}\right)(1 - H[u_l])\right] \\ =& \widetilde{f}^+_{i+1/2,j,l,m} + \widetilde{f}_{i+1/2,j,l,m}, \end{aligned} \tag{10}$$

where $\widetilde{f}^+_{i+1/2,j,l,m}$ is related to equilibrium state integration and $\widetilde{f}_{i+1/2,j,l,m}$ is related to the initial distribution. With the variation of the ratio between evolving time t (i.e., the time step in the computation) and collision time τ, the above interface distribution function provides a self-conditioned multiple scale solution across different flow regimes. After the interface distribution function is determined, the corresponding fluxes of conservative flow variables are evaluated through

$$\mathbf{F}_{i+1/2} = \int u_l f(0,0,t,u_l,v_m,\xi)\psi du dv d\xi.$$

Inside each control volume, the collision term $Q(f)$ is to be determined for the update of particle distribution function in Eq. (6). In the unified scheme, the numerical treatment of $Q(f)$ is based on the full Boltzmann collision term and the Shakhov model. For the full Boltzmann collision term, the fast spectral method is employed [33–35], which is an explicit technique. To overcome the stiffness of the Boltzmann collision term, especially in the continuum limit, an explicit-implicit collision operator with the inclusion of the Shakhov relaxation term is introduced as

$$\int_{t^n}^{t^{n+1}} Q(f_{i,j,l,m})dt = \beta^n \Delta t\, Q(f^n_{i,j}, f^n_{i,j})_{l,m} + (1 - \beta^n)\Delta t \frac{f^{(n+1)+}_{i,j,l,m} - f^{n+1}_{i,j,l,m}}{\tau^{n+1}_{i,j}}. \tag{11}$$

In the computation, Eq. (5) can be solved first, and its solution can be used for the construction of the Shakhov equilibrium state in Eq. (11) at t^{n+1}. As analyzed qualitatively in Eq. (10), the contributions from the initial distribution and equilibrium state are proportional to the factors $e^{-t/\tau}$ and $1 - e^{-t/\tau}$ respectively within an evolving process. Thus, the adjustment coefficient here can be defined as

$$\beta = \exp(-\Delta t/\tau_{i,j}),$$

where Δt is the time step and $\tau_{i,j}$ is the local collision time. This procedure plays an equivalent role as the penalty method proposed in [36].

3.2. Numerical analysis of unified gas kinetic scheme

In this part, a brief numerical analysis of UGKS will be presented. We start from homogeneous problem first. In this case, the solution algorithm of UGKS in Eq. (6) becomes,

$$f^{n+1} = f^n + \beta^n \Delta t Q(f^n, f^n) + (1-\beta^n)\Delta t \frac{f^{(n+1)+} - f^{n+1}}{\tau^{n+1}}. \tag{12}$$

Here we omit subscripts referring to grid index for simplicity. As is known, the Boltzmann collision integration can be divided into gain $Q_+(f,f)$ and loss term $Q_-(f,f)$, which writes,

$$Q_+(f,f) = \int_{\mathcal{R}^3}\int_{\mathcal{S}^2} \left[f(\mathbf{u}')f(\mathbf{u}_1')\right]\mathcal{B}(\cos\theta, |\mathbf{u}-\mathbf{u_1}|)d\mathbf{\Omega}d\mathbf{u}_1,\ \ Q_-(f,f) = \nu f,$$

where $\nu = \int_{\mathcal{R}^3}\int_{\mathcal{S}^2} f(\mathbf{u}_1)\mathcal{B}(\cos\theta, |\mathbf{u}-\mathbf{u_1}|)d\mathbf{\Omega}d\mathbf{u}_1$ is collision frequency. Thus, Eq. (12) can be rewritten as

$$\begin{aligned} f^n =& \frac{1-\Delta t \nu^{n-1}\beta^{n-1}}{1+\Delta t\left(1-\beta^{n-1}\right)/\tau^n} f^{n-1} + \frac{\Delta t \beta^{n-1}}{1+\Delta t\left(1-\beta^{n-1}\right)/\tau^n} Q_+^{n-1} \\ &+ \frac{\Delta t\left(1-\beta^{n-1}\right)/\tau^n}{1+\Delta t\left(1-\beta^{n-1}\right)/\tau^n} f^{(n)+}. \end{aligned} \tag{13}$$

Starting from initial distribution f^0, the numerical solution of UGKS gives

$$\begin{aligned} f^n =& \prod_{i=0}^{n-1}\left(1 - \frac{\left(1-\beta^i\right)/\tau^{i+1} + \nu^i\beta^i}{1+\Delta t\left(1-\beta^i\right)/\tau^{i+1}}\Delta t\right) f^0 \\ &+ \sum_{j=0}^{n-1} \frac{\Delta t \beta^j Q_+^j}{1-\Delta t \nu^j \beta^j} \prod_{i=j}^{n-1} \frac{1-\Delta t\nu^i\beta^i}{1+\Delta t\left(1-\beta^i\right)/\tau^{i+1}} \\ &+ \sum_{j=0}^{n-1} \frac{\Delta t\left(1-\beta^j\right)/\tau^{j+1}}{1-\Delta t\left(1-\beta^j\right)/\tau^{j+1}} f^+ \prod_{i=j}^{n-1} \frac{1-\Delta t\nu^i\beta^i}{1+\Delta t\left(1-\beta^i\right)/\tau^{i+1}}. \end{aligned} \tag{14}$$

When Δt approaches to zero, and assuming a local constant relaxation time τ, the coefficient series converge to

$$\begin{aligned} &\prod_{i=0}^{n-1}\left(1 - \frac{\left(1-\beta^i\right)/\tau + \nu^i\beta^i}{1+\Delta t\left(1-\beta^i\right)/\tau}\Delta t\right) \\ =& \exp\left[-\sum_{i=0}^{n-1}\Delta t\frac{\left(1-\beta^i\right)/\tau + \nu^i\beta^i}{1+\Delta t\left(1-\beta^i\right)/\tau} + \sum_{i=0}^{n-1}\ln\left(1 - \frac{\left(1-\beta^i\right)/\tau + \nu^i\beta^i}{1+\Delta t\left(1-\beta^i\right)/\tau}\Delta t\right)\right. \\ &\left. + \sum_{i=0}^{n-1}\frac{\left(1-\beta^i\right)/\tau + \nu^i\beta^i}{1+\Delta t\left(1-\beta^i\right)/\tau}\Delta t\right] \\ \to& \exp\left(-\int_0^t \left(\nu(f)\beta + \frac{1-\beta}{\tau}\right)dt'\right). \end{aligned} \tag{15}$$

With the regularity of gain term Q_+ in the Boltzmann collision integration [37], the solution provided by UGKS in Eq. (14) becomes

$$\begin{aligned} f(t) &= f_0 e^{-\int_0^t\left(\nu\beta + \frac{1-\beta}{\tau}\right)dt'} + \int_0^t \left(\beta Q_+(f,f) + \frac{1-\beta}{\tau}f^+\right) e^{-\int_{t'}^t\left(\nu\beta+\frac{1-\beta}{\tau}\right)dt''}dt' \\ &= f_0 e^{-\int_0^t \nu dt'} + \int_0^t Q_+(f,f)e^{-\int_{t'}^t \nu dt''}dt', \end{aligned} \tag{16}$$

which is the exact solution of Boltzmann equation.

For inhomogeneous case, the flux function will contribute to the flow evolution. For brevity, one-dimensional case is considered, and the solution algorithm of UGKS in Eq. (6) becomes

$$f_{i,l}^{n+1} = f_{i,l}^{n} + \frac{1}{\Delta x}\int_{t^n}^{t^{n+1}} u_l(f_{i-1/2,l} - f_{i+1/2,l})dt + \beta^n \Delta t Q(f_i^n, f_i^n)_l + (1-\beta^n)\Delta t \frac{f_{i,l}^{(n+1)+} - f_{i,l}^{n+1}}{\tau_i^{n+1}}, \tag{17}$$

where the time-dependent solution of distribution function at cell interface in Eq. (10) writes,

$$\begin{aligned} f(0,t,u_l,\xi) = &\left(1-e^{-t/\tau}\right) f_0^+ \\ &+ \left(\tau(-1+e^{-t/\tau}) + te^{-t/\tau}\right)\bar{a}^{L,R}u_l f_0^+ \\ &+ \tau\left(t/\tau - 1 + e^{-t/\tau}\right)\bar{A} f_0^+ \\ &+ e^{-t/\tau}\left[\left(f_{i+1/2,l}^{L} - u_l t\sigma_{i,l}\right) H[u_l] \right. \\ &\left. + \left(f_{i+1/2,l}^{R} - u_l t\sigma_{i+1,l}\right)(1-H[u_l])\right]. \end{aligned} \tag{18}$$

Let us consider two limiting flow regimes first. In the collisionless limit where $\tau \to \infty$, the relation $\Delta t \ll \tau$ is satisfied, and the interface distribution in Eq. (18) becomes

$$f(0,t,u_l,\xi) = \left(f_{i+1/2,l}^{L} - u_l t\sigma_{i,l}\right) H[u_l] + \left(f_{i+1/2,l}^{R} - u_l t\sigma_{i+1,l}\right)(1-H[u_l]), \tag{19}$$

and Eq. (17) reduces to

$$\begin{aligned} f_{i,l}^{n+1} = f_{i,l}^{n} + \frac{1}{\Delta x}\left[\left(\Delta t f_{i-1/2,l}^{L} - \frac{1}{2}\Delta t^2 u_l \sigma_{i-1,l}\right) H[u_l]\right. \\ + \left(\Delta t f_{i-1/2,l}^{R} - \frac{1}{2}\Delta t^2 u_l \sigma_{i,l}\right)(1-H[u_l]) \\ - \left(\Delta t f_{i+1/2,l}^{L} - \frac{1}{2}\Delta t^2 u_l \sigma_{i,l}\right) H[u_l] \\ \left. - \left(\Delta t f_{i+1/2,l}^{R} - \frac{1}{2}\Delta t^2 u_l \sigma_{i+1,l}\right)(1-H[u_l])\right], \end{aligned} \tag{20}$$

which is a second-order upwind scheme for free molecular flow.

For the continuum flow, we consider a resolved case where there exist continuous distributions of flow variables and their derivatives inside the domain. Therefore, reconstruction technique used in Eq. (18) is equivalent with central interpolation, and the interface solution becomes

$$\begin{aligned} f(0,t,u_l,\xi) = &\left(1-e^{-t/\tau}\right) f_0^+ \\ &+ \left(\tau(-1+e^{-t/\tau}) + te^{-t/\tau}\right)\bar{a}u_l f_0^+ \\ &+ \tau\left(t/\tau - 1 + e^{-t/\tau}\right)\bar{A} f_0^+ \\ &+ e^{-t/\tau}\left(f_{i+1/2,l} - u_l t\sigma_{i+1/2,l}\right). \end{aligned} \tag{21}$$

In the Navier-Stokes regime, the particle distribution follows the first order Chapman-Enskog expansion with respect to a small factor ϵ,

$$f = f^{(0)} + f^{(1)}\epsilon + O(\epsilon^2),$$

which is equivalent with the successive form of the Shakhov equation [38],

$$f = f^+ - \tau(f_t^+ + uf_x^+) + O(\tau^2). \tag{22}$$

To pursue a Navier-Stokes flow, the interface distribution in Eq. (21) should follow

$$f(0,t,u_l,\xi) = f_0^+ - (\tau(\bar{a}u + \bar{A}) + t\bar{A}) f_0^+, \tag{23}$$

where the factor $e^{-t/\tau}$ approaches to zero. The solution algorithm in Eq. (17) goes to

$$f_{i,l}^{n+1} = f_{i,l}^{n} + \frac{1}{\Delta x}\int_{t^n}^{t^{n+1}} u_l(f_{i-1/2,l} - f_{i+1/2,l})dt + \Delta t \frac{f_{i,l}^{(n+1)+} - f_{i,l}^{n+1}}{\tau_i^{n+1}}, \tag{24}$$

which can be rewritten as

$$f_{i,l}^{n+1} = f_{i,l}^{(n+1)+} - \tau_i^{n+1}\frac{f_{i,l}^{n+1} - f_{i,l}^{n}}{\Delta t} - \tau_i^{n+1}\frac{\int_{t^n}^{t^{n+1}} u_l(f_{i-1/2,l} - f_{i+1/2,l})dt}{\Delta t \Delta x}. \tag{25}$$

Following the strategy given in Eq. (25), the Navier-Stokes distribution in the UGKS is recovered,

$$f_{i,l}^{n} = f_{i,l}^{(n)+} + O(\Delta x^2) - \tau\left(\frac{\partial}{\partial t}f_{i,l}^{(n)+} + u_l\frac{\partial}{\partial x}f_{i,l}^{(n)+} + O(\Delta t, \Delta x^2)\right), \tag{26}$$

and the initial distribution function interpolated to cell interface in Eq. (21) is

$$\begin{aligned} f(0,0,u_l,\xi) =& f_{i,l}^{n} + \frac{1}{2}\Delta x\frac{\partial}{\partial x}f_{i,l}^{n} \\ =& f_{i,l}^{(n)+} - \tau\left(\frac{\partial}{\partial t}f_{i,l}^{(n)+} + u_l\frac{\partial}{\partial x}f_{i,l}^{(n)+}\right) \\ &+ \frac{\partial}{\partial x}\left(f_{i,l}^{(n)+} - \tau\left(\frac{\partial}{\partial t}f_{i,l}^{(n)+} + u_l\frac{\partial}{\partial x}f_{i,l}^{(n)+}\right)\right)\frac{1}{2}\Delta x \\ &+ O(\Delta x^2, \tau\Delta t, \tau\Delta x^2) \\ =& f_{i+1/2,l}^{(n)+} - \tau\left(\frac{\partial}{\partial t}f_{i+1/2,l}^{(n)+} + u_l\frac{\partial}{\partial x}f_{i+1/2,l}^{(n)+}\right) + O(\tau\Delta t, \Delta x^2). \end{aligned} \tag{27}$$

By using the above solution as initial state $f_{i+1/2,l}$ in the integral solution in Eq. (21), it turns,

$$\begin{aligned} f(0,t,u_l,\xi) =& f^{+}(0,0,u_l,\xi) - (\tau(\bar{a}u_l + \bar{A}) + t\bar{A})f^{+}(0,0,u_l,\xi) \\ &- \tau t e^{-t/\tau}u_l\frac{\partial}{\partial x}\left((\bar{a}u_l + \bar{A})f^{+}(0,0,u_l,\xi)\right) + O(\tau\Delta t, \Delta t^2, \Delta x^2) \\ =& f^{+}(0,t,u_l,\xi) - \tau\left(\frac{\partial}{\partial t}f^{+}(0,t,u_l,\xi) + u_l\frac{\partial}{\partial x}f^{+}(0,t,u_l,\xi)\right) + O(\tau\Delta t, \Delta t^2, \Delta x^2). \end{aligned} \tag{28}$$

The Navier-Stokes equations can be fully obtained by taking conservative moments of Eq. (24),

$$\begin{aligned} &\frac{\partial\rho}{\partial t} + \frac{\partial(\rho U)}{\partial x} = O\left(\tau\Delta t, \Delta t^2, \Delta x^2\right), \\ &\frac{\partial(\rho U)}{\partial t} + \frac{\partial}{\partial x}\left(\rho U^2 + P - \frac{4}{3}\mu\frac{\partial}{\partial x}U\right) = O\left(\tau\Delta t, \Delta t^2, \Delta x^2\right), \\ &\frac{\partial(\rho E)}{\partial t} + \frac{\partial}{\partial x}\left((\rho E + P)U - \frac{4}{3}\mu U\frac{\partial}{\partial x}U - \kappa\frac{\partial}{\partial x}T\right) = O\left(\tau\Delta t, \Delta t^2, \Delta x^2\right), \end{aligned} \tag{29}$$

with the coefficients of viscosity $\mu = \tau p$ and heat conduction $\kappa = c_p\tau p/Pr$.

As demonstrated, the UGKS is an efficient method to describe Navier-Stokes dynamics. Moreover, as $\tau \to 0$, the dissipative structure narrows down to discontinuity in the flow field due to intensive intermolecular collisions. With limited numerical spatial and temporal resolution, the effects of physical viscosity and conductivity are replaced by numerical dissipation. In this way, the UGKS becomes a second order shock capturing scheme for the Euler equations with $O(\Delta t^2, \Delta x^2)$.

The above analysis illustrates two limiting cases of UGKS. However, it is challenging to analyze the validity and accuracy of UGKS in theory between these two ends, mainly due to the lack of knowledge in the transition regime. From individual particle transport to collective fluid behavior, how many degrees of freedom and which variables should be used to model the flow dynamics within the coarse-graining process still remain as open problems. In spite of progresses of asymptotic techniques starting from Boltzmann and its model equation, there is no clearly defined modeling scale for extended hydrodynamic equations, and the convergence of higher order expansion is questionable in itself. Therefore, the validation of UGKS in the transition regime at a relative large modeling scale has to rely partly on the numerical solutions with respect to the results from Boltzmann or DSMC methods with the finest kinetic scale resolution. As presented in [27], the homogeneous relaxation problem is tested for different kinds of particle distribution function, i.e., anisotropic Maxwellian, double half-normal distribution with discontinuity, and tailored asymmetric ones. The results indicate that after $t_c = 0.2\tau$ for moderate initial non-equilibrium distribution, and $t_c = 2\tau$ for extremely one, the deviations between full Boltzmann and Shakhov solutions become marginal, and the solution algorithm in Eq. (12) quickly becomes equivalent with

$$f^{n+1} = f^{n} + \beta^{n}\Delta t\frac{f^{(n)+} - f^{n}}{\tau^{n}} + (1-\beta^{n})\Delta t\frac{f^{(n+1)+} - f^{n+1}}{\tau^{n+1}}. \tag{30}$$

In other words, the Boltzmann collision operator only plays a significant role at the very early stage of evolving process in highly rarefied region. Generally, for inhomogeneous problem during this interval with $t < t_c$, the interface distribution approaches to particle free transport formula in Eq. (19), and the UGKS becomes an upwind scheme for Boltzmann equation,

$$\begin{aligned} f_{i,l}^{n+1} = f_{i,l}^{n} + \frac{1}{\Delta x}\Bigg[& \left(\Delta t f_{i-1/2,l}^{L} - \frac{1}{2}\Delta t^2 u_l \sigma_{i-1,l}\right) H\left[u_l\right] \\ & + \left(\Delta t f_{i-1/2,l}^{R} - \frac{1}{2}\Delta t^2 u_l \sigma_{i,l}\right)\left(1 - H\left[u_l\right]\right) \\ & - \left(\Delta t f_{i+1/2,l}^{L} - \frac{1}{2}\Delta t^2 u_l \sigma_{i,l}\right) H\left[u_l\right] \\ & - \left(\Delta t f_{i+1/2,l}^{R} - \frac{1}{2}\Delta t^2 u_l \sigma_{i+1,l}\right)\left(1 - H\left[u_l\right]\right)\Bigg] + \Delta t Q\left(f_i^n, f_i^n\right)_l. \end{aligned} \tag{31}$$

And after several relaxation times, the UGKS provide following numerical algorithm in the transition regime,

$$f_{i,l}^{n+1} = f_{i,l}^{n} + \frac{1}{\Delta x}\int_{t^n}^{t^{n+1}} u_l (f_{i-1/2,l} - f_{i+1/2,l}) dt + \beta^n \Delta t \frac{f_{i,l}^{(n)+} - f_{i,l}^{n+1}}{\tau_i^n} + (1-\beta^n)\Delta t \frac{f_{i,l}^{(n+1)+} - f_{i,l}^{n+1}}{\tau_i^{n+1}}, \tag{32}$$

which is a consistent full Shakhov solution.

Since the numerical experiments in [27] mainly target homogeneous cases, here we will provide a numerical experiment of shear layer [39] to demonstrate the performance of UGKS in inhomogeneous cases over the whole Knudsen regimes. The initial condition of argon gas is set as

$$(n, U, V, T) = \begin{cases} \left(1.33291 \times 10^{25}/\mathrm{m}^3, 0, 408.05\ \mathrm{m/s}, 400\ \mathrm{K}\right), & x \le 0, \\ \left(1.33291 \times 10^{25}/\mathrm{m}^3, 0, -408.05\ \mathrm{m/s}, 200\ \mathrm{K}\right), & x > 0. \end{cases} \tag{33}$$

The Knudsen number $Kn = \ell/L_\infty$ is fixed as 5.0×10^{-3} regarding to the reference temperature of 300 K, with mean free path $\ell = 1.0 \times 10^{-7}$ m, mean collision time $\tau_{ph} = 2.5 \times 10^{-10}$ s and $L_\infty = 2.0 \times 10^{-5}$ m. The reference viscosity of argon is $\mu = 2.117 \times 10^{-5}$ Pa·s at $T = 273$ K, and the viscosity coefficient depends on the temperature with a power $\omega = 0.81$. The density, velocity, temperature, heat flux, as well as velocity distribution functions at different times $t_1 = \tau_{ph}$, $t_2 = 10\tau_{ph}$, $t_3 = 100\tau_{ph}$, $t_4 = 781.76\tau_{ph}$ have been obtained, with a changeable cell size in order to identify the shear solution on different scales. The UGKS with Boltzmann-Shakhov explicit-implicit collision operator in Eq. (17) (denoted with B+S) and complete Shakhov term in Eq. (32) (denoted with Full S) are used simultaneously for comparison. The numerical results are presented in Fig. 1, 2, 3, and 4 respectively, with the reference solutions of DSMC and Navier-Stokes solver [31] for evaluating the performance of UGKS over the whole Knudsen regime. With the incorporation of full Boltzmann collision term, the UGKS provides more reliable solutions compared to complete Shakhov ones in the free molecular and early transition regimes, which is clearly demonstrated in Fig. 1 and 2, especially in Fig. 1d and 2d for the particle distribution function along $V-$velocity at the center of flow domain. Besides, with the explicit-implicit strategy, it does not lose the validity to capture the asymptotic-preserving Navier-Stokes solutions, as presented in Fig. 4. By comparing UGKS solution with the DSMC and Navier-Stokes solutions, it is clear that UGKS is a multiscale solver from the kinetic to hydrodynamic regimes, and works effectively in the transition regime. In general, the direct modeling on the mesh size and time step scales ensures the capturing of scale variation dynamics from non-equilibrium to equilibrium flow physics. The UGKS algorithm can be regarded as a kind of discretized governing equations based on the representation of physical laws in a discretized space.

3.3. Gas kinetic scheme with continuous velocity space for near-continuum flow

In continuum flow with intensive intermolecular collisions, the particle distribution function is close to a local thermodynamic equilibrium, and the Navier-Stokes equations are valid to describe macroscopic fluid motion. In this case, it is straightforward to apply the first-order Chapman-Enskog expansion to construct the corresponding distribution function, and thus only macroscopic conservative variables need to be stored and updated. In the Chapman-Enskog expansion, the particle distribution function is expanded around the equilibrium state with respect to a small factor ϵ,

$$f = f^{(0)} + f^{(1)}\epsilon + f^{(2)}\epsilon^2 + \cdots,$$

which is equivalent to the successive expansion of the Shakhov model [38],

$$f = f^{+} - \tau \frac{D}{Dt} f^{+} + \tau \frac{D}{Dt}\left(\tau \frac{D}{Dt} f^{+}\right) + \cdots, \tag{34}$$

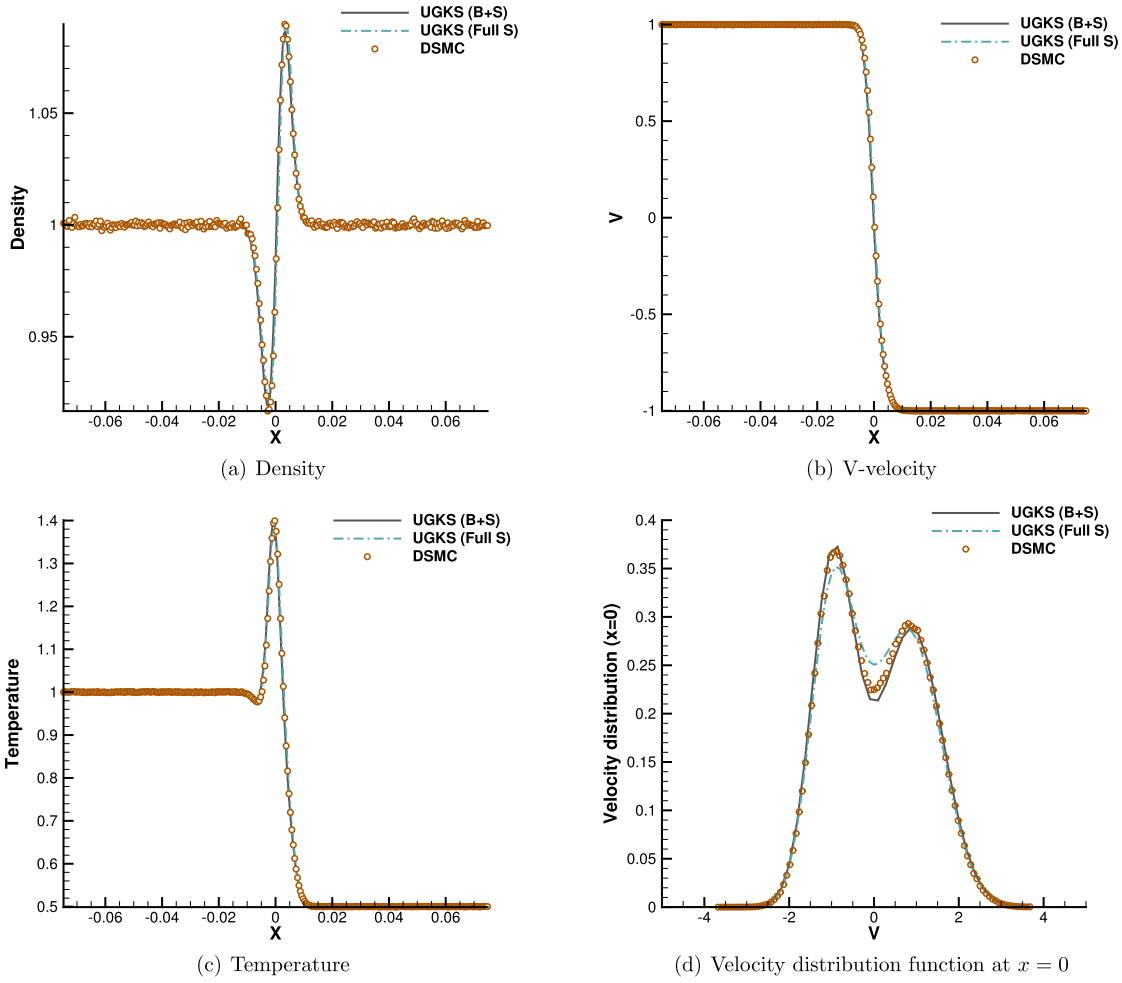

(a) Density (b) V-velocity

(c) Temperature (d) Velocity distribution function at $x = 0$

Fig. 1. Numerical results of UGKS with Boltzmann-Shakhov explicit-implicit operator, UGKS with Shakhov term only, as well as DSMC for the shear layer problem at $t = \tau_{ph}$. For UGKS, $dx/\ell = 0.1$, $dt = 1.96 \times 10^{-3}\tau_{ph}$. (For interpretation of the colors in the figures, the reader is referred to the web version of this article.)

where $D/Dt = \partial/\partial t + u\partial/\partial x + v\partial/\partial y$ is the total derivative. For the first order truncation with respect to the collision time τ, the distribution function f becomes,

$$f = f^+ - \tau(f_t^+ + uf_x^+ + vf_y^+) + O(\tau^2).$$

Following this procedure, in the gas kinetic scheme with continuous particle velocity space, we can expand the equilibrium distribution function around the interface,

$$f^+(x,t) = f^+(x=0,t=0)\left(1 + a^{l,r}x + b^{l,r}y + At\right),$$

where f_0^+ is the equilibrium distribution at $(x=0, y=0, t=0)$. The particle distribution function f_0 in Eq. (7) at the beginning of each time step can be constructed as [31],

$$f_0 = \begin{cases} f_0^{+(l)}\left(1 + a^l x + b^l y - \tau\left(a^l u + b^l v + A^l\right)\right), & x \le 0 \\ f_0^{+(r)}\left(1 + a^r x + b^r y - \tau\left(a^r u + b^r v + A^r\right)\right), & x > 0 \end{cases} \tag{35}$$

where $f_0^{+(l)}$ and $f_0^{+(r)}$ are the equilibrium distribution functions which have one to one correspondence with the macroscopic flow variables $\mathbf{W}_{i+1/2}^{l,r}$ at left and right sides of the interface. The space-time derivatives $(a^{l,r}, b^{l,r}, A^{l,r})$ depend on the reconstructed spatial slopes $\nabla\mathbf{W}^{l,r}$ of macroscopic flow variables at the left and right sides of a cell interface, which

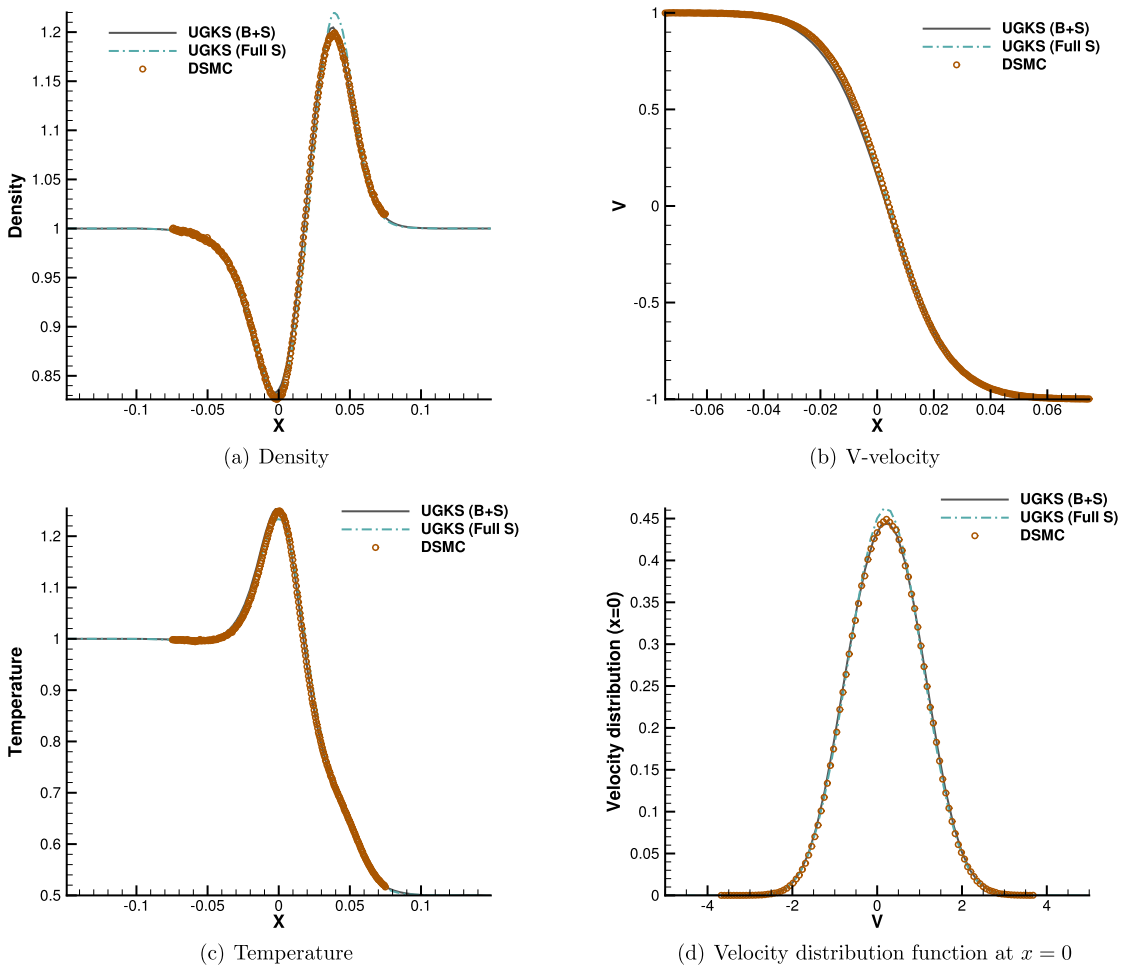

(a) Density (b) V-velocity

(c) Temperature (d) Velocity distribution function at $x = 0$

Fig. 2. Numerical results of UGKS with Boltzmann-Shakhov explicit-implicit operator, UGKS with Shakhov term only, as well as DSMC for the shear layer problem at $t = 10\tau_{ph}$. For UGKS, $dx/\ell = 0.4$, $dt = 6.61 \times 10^{-2}\tau_{ph}$.

are determined in the similar way given in Sec. 3.1. After the determination of the equilibrium distribution function, its spatial derivatives $a^{l,r}$ can be evaluated via,

$$\int a^l f_0^{+(l)} \psi du dv d\xi = \nabla_x \mathbf{W}^l,$$
$$\int a^r f_0^{+(r)} \psi du dv d\xi = \nabla_x \mathbf{W}^r,$$
$$\int b^l f_0^{+(l)} \psi du dv d\xi = \nabla_y \mathbf{W}^l,$$
$$\int b^r f_0^{+(r)} \psi du dv d\xi = \nabla_y \mathbf{W}^r.$$

Then the time derivative $A^{l,r}$ can be obtained through,

$$\begin{aligned}\int A^{l,r} f_0^{+(l,r)} \psi du dv d\xi &= -\int \left(u \frac{\partial f^{+(l,r)}}{\partial x} + v \frac{\partial f^{+(l,r)}}{\partial y} \right) \psi du dv d\xi \\ &= -\int (a^{l,r} u + b^{l,r} v) f_0^{+(l,r)} \psi du dv d\xi.\end{aligned}$$

Since the equilibrium distribution function f^+ around a cell interface can be constructed in the same way as that in Eq. (9), the corresponding interface distribution function becomes,

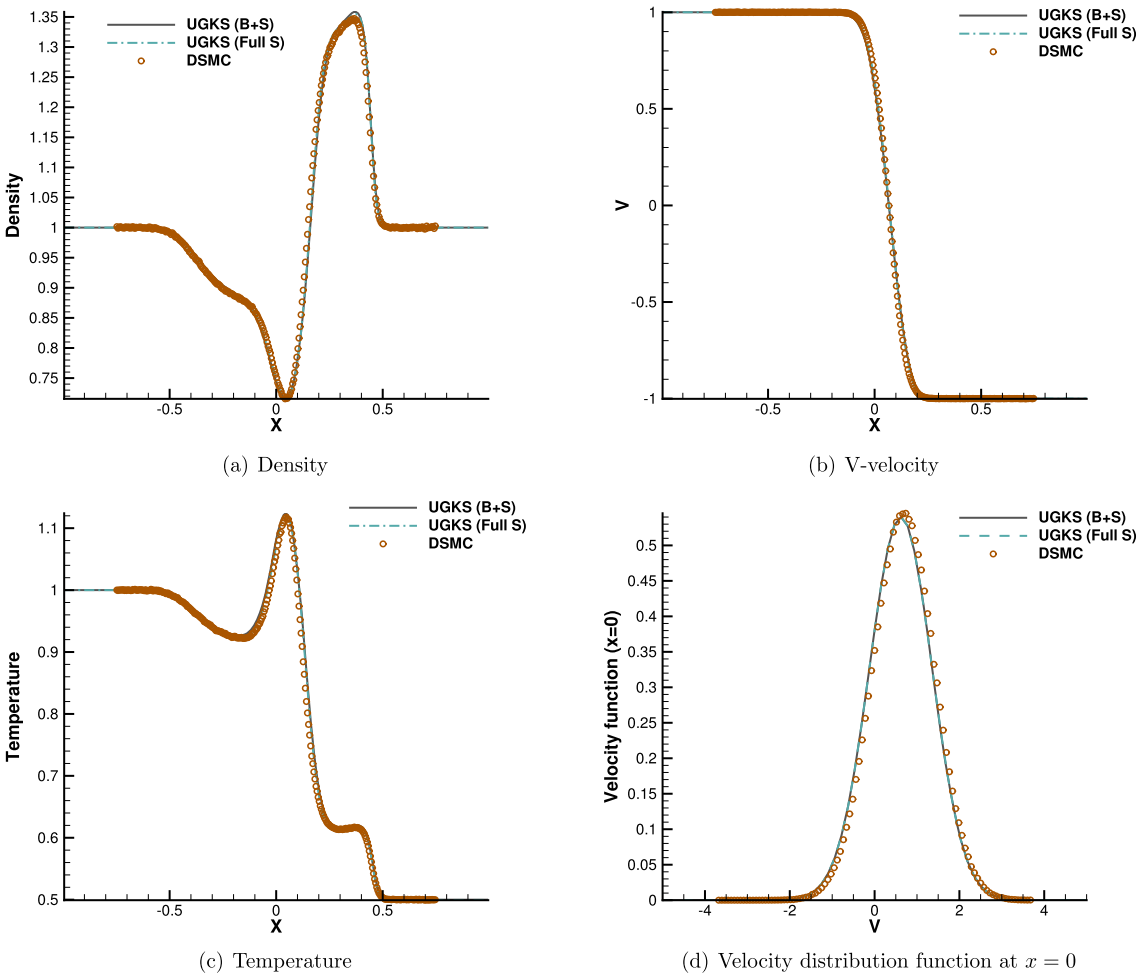

(a) Density (b) V-velocity

(c) Temperature (d) Velocity distribution function at $x = 0$

Fig. 3. Numerical results of UGKS with Boltzmann-Shakhov explicit-implicit operator, UGKS with Shakhov term only, as well as DSMC for the shear layer problem at $t = 100\tau_{ph}$. For UGKS, $dx/\ell = 2$, $dt = 3.78 \times 10^{-1}\tau_{ph}$.

$$
\begin{aligned}
f(0,0,t,u,v,\xi) = & \left(1-e^{-t/\tau}\right) f_0^+ \\
& + \left(\tau(-1+e^{-t/\tau}) + te^{-t/\tau}\right)(\bar{a}^{L,R}u + \bar{b}v) f_0^+ \\
& + \tau\left(t/\tau - 1 + e^{-t/\tau}\right)\bar{A} f_0^+ \\
& + e^{-t/\tau}\Big\{[1-(t+\tau)(ua^l+vb^l)]H[u] f_0^{+(l)} \\
& + [1-(t+\tau)(ua^r+vb^r)][1-H[u]] f_0^{+(r)}\Big\} \\
& + e^{-t/\tau}\left[-\tau A^l H[u] f_0^{+(l)} - \tau A^r (1-H[u]) f_0^{+(r)}\right].
\end{aligned}
\tag{36}
$$

The interface distribution function here is a continuous function of particle velocity (u, v), and the fluxes for macroscopic variables can be obtained by taking moments of the above distribution function analytically.

3.4. Adaptive unified gas kinetic scheme

In a multiscale flow problem, in order to overcome the computational deficiency and memory burden from a large amount of discretized velocity points, it is feasible to combine both continuum and rarefied flow solvers into a single framework with an adaptive continuous-discrete velocity transformation. As shown in Fig. 5, in near-equilibrium flow regions, the particle distribution function (PDF) is formulated with a continuous velocity space based on the Chapman-Enskog expansion, and only macroscopic flow variables are updated. In non-equilibrium regions, the AUGKS switches to a discretized velocity space to follow the evolution of particle distribution function. The continuous and discrete velocity spaces are connected

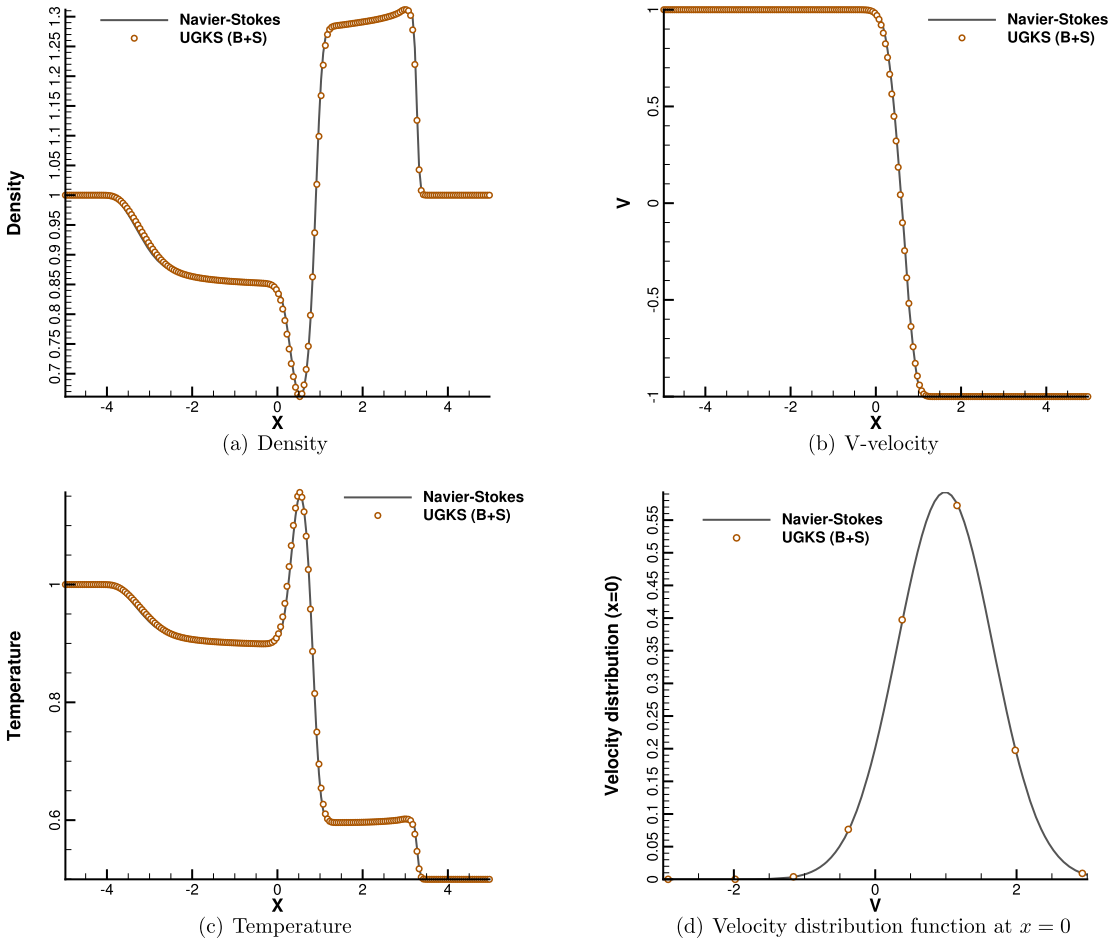

Fig. 4. Numerical results of UGKS with Boltzmann-Shakhov explicit-implicit operator, UGKS with Shakhov term only, as well as DSMC for the shear layer problem at $t = 781.76\tau_{ph}$. For UGKS, $dx/\ell = 10$, $dt = 1.89\tau_{ph}$.

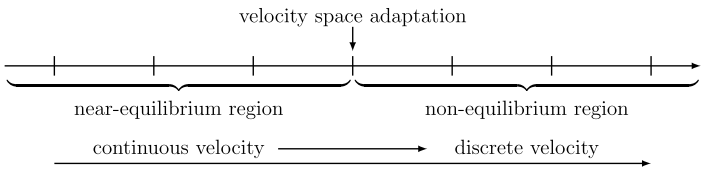

Fig. 5. Schematic of the adaptive scheme for multiscale flow.

with an adaptation interface, at which the continuous solution of distribution function is sorted onto discretized velocity points.

In the detailed numerical scheme, the macroscopic conservative variables are updated in Eq. (5), while in the non-equilibrium region the particle distribution function is updated in Eq. (6). Near the adaptation interface, at every time step t^n, if there is no recorded discretized distribution function at t^{n-1} in the newly formed "non-equilibrium" cell (i, j), a local discretized velocity mesh will be generated, where the particle distribution function at velocity point (l, m) is given by the discrete Chapman-Enskog expansion,

$$f_{i,j,l,m} = f^{+}_{0(i,j,l,m)}[1 - \tau(au_l + bv_m + A)], \tag{37}$$

where the spatial derivatives (a, b) are related to the averaged reconstructed slopes of macroscopic variables $\nabla\mathbf{W} = (\nabla\mathbf{W}^l + \nabla\mathbf{W}^r)/2$, and then the coefficients (a, b, A) can be determined in the same way as that in Sec. 3.2. In the current scheme, the velocity mesh is generated within

$$u \in [U - 3\sqrt{RT}, U + 3\sqrt{RT}],\ v \in [V - 3\sqrt{RT}, V + 3\sqrt{RT}],$$

where (U, V) is macroscopic flow velocity, T is temperature, and R is the gas constant.

To update the discretized distribution function in the adjacent cell next to the adaptation interface, the interface distribution function from the continuous GKS solution in Eq. (36) is rewritten into the following discrete form,

$$\begin{aligned} f(0,0,t,u_l,v_m,\xi) = & \left(1-e^{-t/\tau}\right) f_0^+ \\ & + \left(\tau(-1+e^{-t/\tau}) + te^{-t/\tau}\right)(\bar{a}^{L,R}u_l + \bar{b}v_m) f_0^+ \\ & + \tau\left(t/\tau - 1 + e^{-t/\tau}\right)\bar{A} f_0^+ \\ & + e^{-t/\tau}\left\{[1-(t+\tau)(u_l a^l + v_m b^l)]H[u_l] f_0^{+(l)}\right. \\ & \left. + [1-(t+\tau)(u_l a^r + v_m b^r)][1-H[u_l]] f_0^{+(r)}\right\} \\ & + e^{-t/\tau}\left[-\tau A^l H[u_l] f_0^{+(l)} - \tau A^r (1-H[u_l]) f_0^{+(r)}\right], \end{aligned} \tag{38}$$

and then it can be used to determine the fluxes of macroscopic flow variables and particle distribution function. In this way, the fluxes at adaptation interface are fully determined and can be used to update the macroscopic variables in Eq. (5) and particle distribution function in Eq. (6).

In the current scheme, the time step is determined by the CFL condition,

$$\Delta t = \mathrm{CFL}\frac{\Delta x \Delta y}{u_{max}\Delta y + v_{max}\Delta x}, \tag{39}$$

where CFL is the CFL number, and (u_{max}, v_{max}) is the largest particle velocity in x and y directions.

3.5. Switching criterion of velocity space

The accuracy and efficiency of the current adaptive scheme are based on a proper choice of location of velocity space adaptation. The transition from discrete to continuous velocity space must be located in the region where the Navier-Stokes solutions provided by the GKS with a continuous velocity space are still valid. In the past, many empirical parameters for the breakdown of continuum description have been proposed. Bird [4] proposed a parameter $P = D(ln\rho)/Dt/\nu$ for the DSMC simulation of expansion flows, where ρ is gas density and ν is collision frequency, and the breakdown value of P for translational equilibrium is 0.05. Boyd et al. [40] extended the above concept to a gradient-length-local Knudsen number $Kn_{GLL} = \ell|\nabla Q|/Q$, where ℓ is the local mean free path and Q is the macroscopic flow quantity of interest, with a critical value 0.05. Considering the terms in the Chapman-Enskog distribution function, Garcia et al. [41] proposed a breakdown parameter based on dimensionless stress and heat flux $B = max(|\tau^*|, |q^*|)$, with the switching criterion of 0.1. Levermore et al. [22] developed non-dimensional matrices from the moments of particle distribution function. The tuning parameter ΔV is then defined as the deviation of the eigenvalues of this matrix from their equilibrium values of unity, with the critical value of 0.25.

Since the particle distribution function takes the Chapman-Enskog expansion in the evolution process of the continuous GKS solver, here we propose an alternative switching criterion of particle velocity space directly from the Chapman-Enskog expansion. For brevity, the one-dimensional case will be used for illustration. When there is no discontinuity inside the flow field, the Chapman-Enskog expansion Eq. (35) gives

$$f(x_0,u,t) = f_0^+[1-\tau(au+A)], \tag{40}$$

where the space-time derivatives a, A can be expanded based on the collision invariants,

$$\begin{aligned} a &= a_1 + a_2 u + a_3 \frac{1}{2}(u^2+\xi^2) = a_\alpha \psi_\alpha, \\ A &= A_1 + A_2 u + A_3 \frac{1}{2}(u^2+\xi^2) = A_\alpha \psi_\alpha. \end{aligned}$$

The equilibrium distribution function f_0^+ is determined by local macroscopic flow variables, and its spatial derivative a can be derived in the same way as given in Sec. 3.1 and 3.2, i.e.,

$$\frac{\partial \mathbf{W}}{\partial x} = \int a f_0^+ \psi du d\xi = M_{\alpha\beta} a_\beta,$$

where ψ is a vector of collision invariants, $M_{\alpha\beta} = \int f_0^+ \psi_\alpha \psi_\beta du d\xi$ and $\mathbf{a} = (a_1, a_2, a_3)^T$. The solution of $\mathbf{a}$ in one-dimensional case writes,

$$a_3 = 4\frac{\lambda^2}{3\rho}\left[2\frac{\partial(\rho E)}{\partial x} - 2U\frac{\partial(\rho U)}{\partial x} + \frac{\partial \rho}{\partial x}\left(U^2 - \frac{3}{2\lambda}\right)\right],$$
$$a_2 = 2\frac{\lambda}{\rho}\left[2\frac{\partial(\rho U)}{\partial x} - U\frac{\partial \rho}{\partial x}\right] - Ua_3,$$
$$a_1 = \frac{1}{\rho}\frac{\partial \rho}{\partial x} - Ua_2 - \frac{1}{2}\left[U^2 + \frac{3}{2\lambda}\right]a_3.$$

In the current scheme, the spatial derivatives are evaluated through

$$\frac{\partial \mathbf{W}}{\partial x} = \max\left[\left(\frac{\partial \mathbf{W}}{\partial x}\right)^L, \left(\frac{\partial \mathbf{W}}{\partial x}\right)^R\right],$$
$$\left(\frac{\partial \mathbf{W}}{\partial x}\right)^L \simeq \frac{\mathbf{W}_i - \mathbf{W}_{i-1}}{\Delta x^-}, \left(\frac{\partial \mathbf{W}}{\partial x}\right)^R \simeq \frac{\mathbf{W}_{i+1} - \mathbf{W}_i}{\Delta x^+}, \tag{41}$$

where $\Delta x^+ = x_{i+1} - x_i$ and $\Delta x^- = x_i - x_{i-1}$ are the distances between adjacent cell centers. The time derivative A is related to the temporal variation of conservative flow variables respectively, and can be evaluated through,

$$\frac{\partial \mathbf{W}}{\partial t} = \int A f_0^+ \psi d\mathbf{u} = -\int u\frac{\partial f_0^+}{\partial x}\psi d\mathbf{u} = -\int a u f_0^+ \psi du d\xi.$$

Generally, the Navier-Stokes equations can be applied when the Chapman-Enskog expansion is a proper approximation of the distribution function in near-equilibrium regime. Therefore, based on the dimensionless collision time and space-time variations, a switching criterion for the velocity space transformation can be defined as

$$B = \hat{\tau}\max(|\hat{a}|, |\hat{A}|), \tag{42}$$

where dimensionless variables are defined as,

$$\hat{\tau} = \frac{\tau(2RT_0)^{1/2}}{L_0}, \hat{a} = aL_0, \hat{A} = \frac{AL_0}{(2RT_0)^{1/2}}, \tag{43}$$

where R is gas constant, L_0 and T_0 are reference length and temperature. The current switching criterion B for particle velocity space will be tested in numerical experiments.

3.6. Summary

The numerical algorithm of the adaptive unified gas kinetic scheme is as following. In the AUGKS, we follow the evolution of both conservative flow variables and particle distribution function. In near-equilibrium flow regions, the particle distribution function is formulated by the Chapman-Enskog expansion with a continuous velocity space, and macroscopic flow variables are updated in Eq. (5). For non-equilibrium flows, besides the update of macroscopic variables, the particle distribution function is updated as well in Eq. (6). The scale-dependent flux function is determined by the particle distribution function at the interface, which comes from the integral solution of kinetic model equation in Eq. (4). In each time step, the domain of continuous and discrete velocity space is specified by Eq. (42), and the corresponding interface fluxes are provided by Eq. (10) with discrete velocity space in UGKS, by Eq. (38) with discrete velocity space in GKS, and by Eq. (36) with continuous velocity space in GKS. The detailed numerical procedures for AUGKS are given in Fig. 6.

4. Numerical experiments

In this section, we are going to test the performance of the current AUGKS. In order to demonstrate the multiscale nature of the algorithm, simulations from continuum Euler and Navier-Stokes to free molecule flow are presented. The following dimensionless flow variables are used in the calculations,

$$\hat{x} = \frac{x}{L_0}, \hat{y} = \frac{y}{L_0}, \hat{\rho} = \frac{\rho}{\rho_0}, \hat{T} = \frac{T}{T_0}, \hat{u}_i = \frac{u_i}{(2RT_0)^{1/2}},$$
$$\hat{U}_i = \frac{U_i}{(2RT_0)^{1/2}}, \hat{f} = \frac{f}{\rho_0(2RT_0)^{3/2}}, \hat{P}_{ij} = \frac{P_{ij}}{\rho_0(2RT_0)}, \hat{q}_i = \frac{q_i}{\rho_0(2RT_0)^{3/2}},$$

where u_i is the particle velocity, U_i is the macroscopic flow velocity, P_{ij} is the stress tensor, q_i is the heat flux. The subscript zero represents the reference state. For simplicity, the hat notation for dimensionless variables will be removed henceforth. Argon gas is used in the simulation with the variable hard sphere (VHS) molecule model, and the dynamic viscosity is related to the Knudsen number in the reference state via

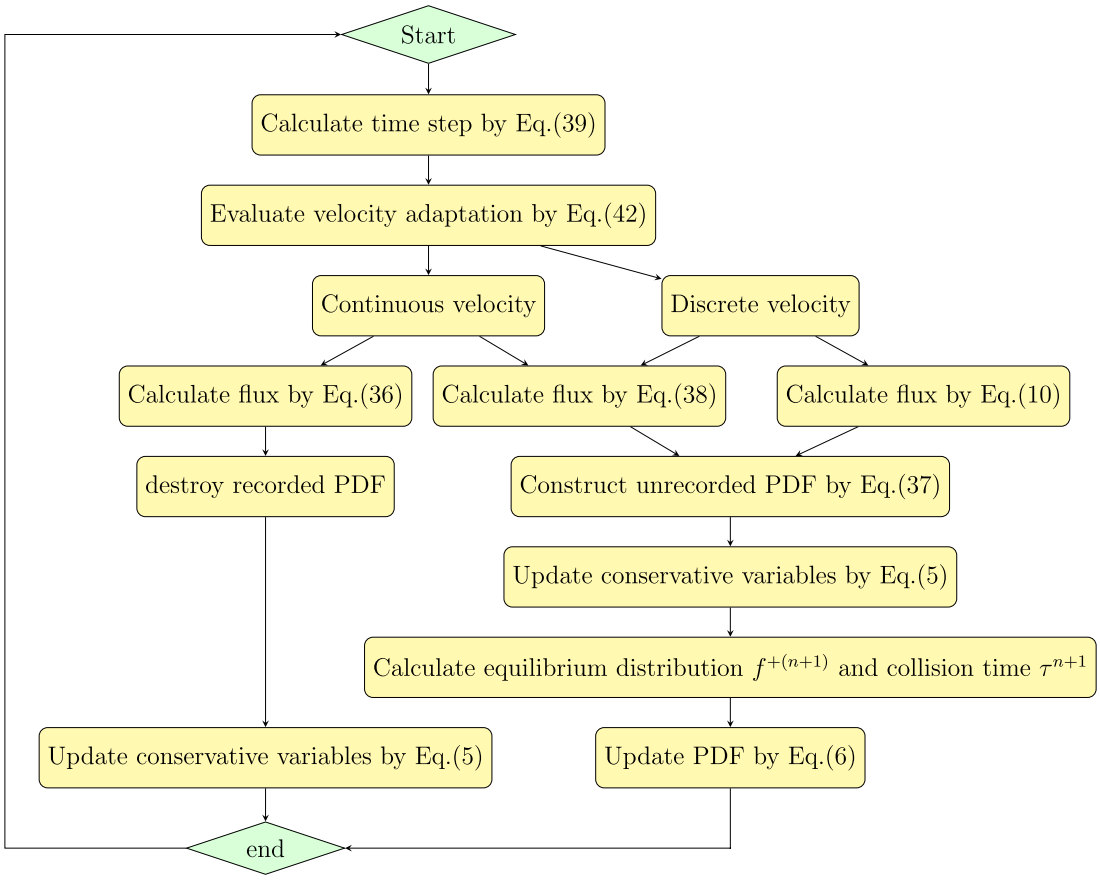

Fig. 6. Numerical algorithm of AUGKS.

$$\mu_{ref} = \frac{5(\alpha+1)(\alpha+2)\sqrt{\pi}}{4\alpha(5-2\omega)(7-2\omega)} Kn_{ref}.$$

In this simulation, we choose $\alpha = 1.0$ and $\omega = 0.5$ to recover a hard sphere molecule, and the viscosity varies with temperature through

$$\mu = \mu_{ref} \left(\frac{T}{T_{ref}} \right)^{\theta},$$

where T_{ref} is the reference temperature and $\theta = 0.81$ is the index of viscosity coefficient.

4.1. Density wave propagation

The first case is the propagation of a density wave. The initial condition is set as

$$\rho = 1.0 + 0.1\sin(2\pi x),\ U = 1.0,\ p = 0.5.$$

The flow domain is $x \in [0, 1]$, with periodic boundary condition. The simulations are performed from reference Knudsen number $Kn = 0.0001$ to 0.1, corresponding to different flow regimes. The velocity space is discretized into 48 uniform points for the update of particle distribution function, and the current criterion value for velocity space transformation is set as $B = 0.0005$. In the AUGKS and UGKS, the collision term is solved here by Eq. (11).

First, we use 200 uniform cells in physical space to simulate this problem with different reference Knudsen numbers. The density profiles at $t = 1.0$ are presented in Fig. 7, with the traveling wave solution of inviscid flow presented as reference. As plotted, in all cases the AUGKS and original UGKS solutions agree with each other very well. In the continuum regime at $Kn = 0.0001$, the numerical scheme and inviscid theory give the equivalent solution. With an increased Knudsen number, the non-equilibrium mechanism dissipates the density inhomogeneity much faster during the wave propagation. As a result, the amplitude of density wave decreases and deviates from the inviscid traveling wave solution. In the rarefied case with $Kn = 0.1$, the amplitude of wave at the output time is only 0.65% of its initial value.

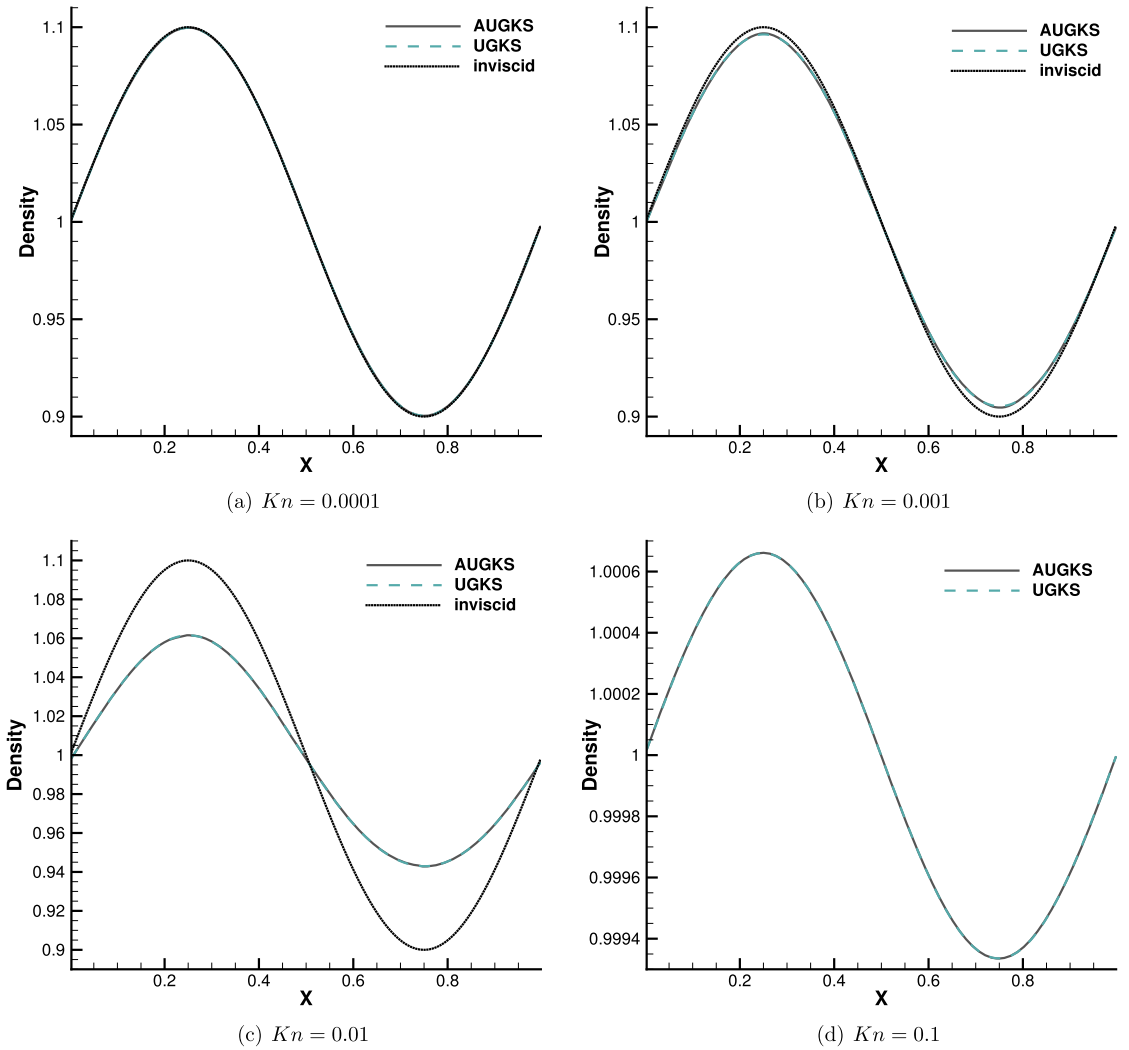

(a) $Kn = 0.0001$ (b) $Kn = 0.001$

(c) $Kn = 0.01$ (d) $Kn = 0.1$

Fig. 7. Density profiles in the wave propagation problem at $t = 1.0$ at different reference Knudsen numbers.

Then, we compare the numerical errors and convergence orders of AUGKS in different flow regimes. In the computation, N uniform cells are used with $N = 10, 20, 40, 80, 160$. The CFL number is set as 0.2. Due to the lack of theoretical traveling wave solutions for viscous flows, the numerical results calculated by UGKS with an extremely fine mesh $N = 1280$ are used to calculate the numerical errors and accuracy of the scheme. The L^1, L^2 and L^∞ errors and convergence orders of the current scheme at from $Kn = 0.0001$ to 0.1 are provided from Table 1 to 4. As analyzed in Sec. 3.2, for near-equilibrium flows, the AUGKS should be of second order accuracy. With the mesh refinement, it can be seen that the expected order of accuracy is obtained. The existing fluctuations of convergence orders at some mesh sizes are mainly due to the numerical errors contained in the reference solutions originally. As the Knudsen number increases to $Kn = 0.1$, the scheme loses second order accuracy. This is because at the moment the collision term in Eq. (11) goes more to the explicit full Boltzmann collision operator part, which is only first order accurate in time. Also the hybridization of Boltzmann-Shakhov collision term and the full Shakhov based interface flux may introduce slight numerical errors in the transition regime, which is shown in Table 4.

Fig. 8 presents the velocity space adaptation inside the flow field at the output instant at different Knudsen numbers. As presented, at $Kn = 0.0001$ the whole flow domain is simulated with continuous velocity space. With increasing Knudsen number, the non-equilibrium region enlarges gradually along with the use of discrete velocity space. At $Kn = 0.001$, the flow domain is divided into some sub-zones, where the particle distribution function in large-slope region is fully resolved with discretized velocity space. In the crest and through regions with relative flat density distribution, the Chapman-Enskog expansion is adopted with a continuous velocity space. With increasing Knudsen number and rarefaction effect, the Navier-Stokes solutions lose its validity, and the non-equilibrium region occupies the whole domain at $Kn = 0.01$.

Table 5 presents the CPU time cost and memory load from the current adaptive scheme and original UGKS method. As shown, the AUGKS is about 157 times faster than UGKS at $Kn = 0.0001$, and saves 94% memory requirement. Since the

Table 1
Errors and convergence orders of AUGKS in the density wave propagation problem at $Kn = 0.0001$.

Mesh size	L^1 error	Order	L^2 error	Order	L^∞ error	Order
1/10	2.291004E-2		8.007182E-3		3.544807E-2	
1/20	5.011979E-3	2.19	1.239875E-3	2.69	7.765276E-3	2.19
1/40	1.124238E-3	2.16	1.975271E-4	2.65	1.770660E-3	2.13
1/80	1.534212E-4	2.87	1.908457E-5	3.37	2.433087E-4	2.86
1/160	2.704649E-5	2.50	2.367716E-6	3.01	4.238944E-5	2.52

Table 2
Errors and convergence orders of AUGKS in the density wave propagation problem at $Kn = 0.001$.

Mesh size	L^1 error	Order	L^2 error	Order	L^∞ error	Order
1/10	2.212397E-2		7.751042E-3		3.463524E-2	
1/20	5.094110E-3	2.19	1.261715E-3	2.62	8.080559E-3	2.10
1/40	1.013216E-3	2.33	1.789057E-4	2.82	1.635674E-3	2.30
1/80	1.597152E-4	2.67	1.998537E-5	3.16	2.623773E-4	2.64
1/160	2.667065E-5	2.58	2.367358E-6	3.08	4.478313E-5	2.55

Table 3
Errors and convergence orders of AUGKS in the density wave propagation problem at $Kn = 0.01$.

Mesh size	L^1 error	Order	L^2 error	Order	L^∞ error	Order
1/10	1.673591E-2		5.943374E-3		2.737731E-2	
1/20	3.917403E-3	2.09	9.823626E-4	2.60	6.770120E-3	2.02
1/40	9.097435E-4	2.11	1.624696E-4	2.60	1.581946E-3	2.10
1/80	1.511126E-4	2.59	1.927517E-5	3.08	2.759125E-4	2.52
1/160	1.821315E-5	3.05	1.635656E-6	3.56	3.587540E-5	2.94

Table 4
Errors and convergence orders of AUGKS in the density wave propagation problem at $Kn = 0.1$.

Mesh size	L^1 error	Order	L^2 error	Order	L^∞ error	Order
1/10	9.502463E-4		3.286562E-4		1.476651E-3	
1/20	2.006481E-4	2.24	4.966555E-5	2.73	3.182716E-4	2.21
1/40	5.142814E-5	1.96	9.031250E-6	2.46	8.098216E-5	1.97
1/80	1.522531E-5	1.76	1.891497E-6	2.26	2.404696E-5	1.75
1/160	5.105088E-6	1.58	4.483010E-7	2.08	8.067447E-6	1.58

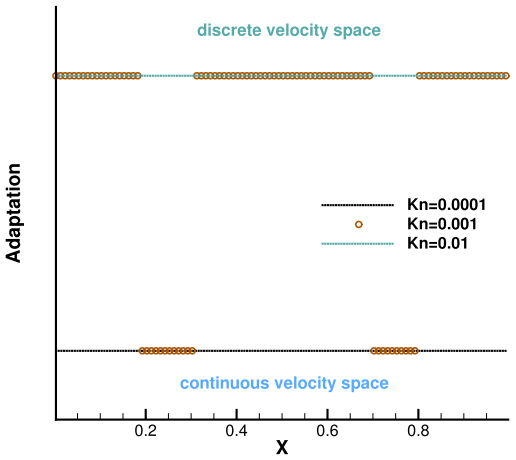

Fig. 8. Velocity space adaptation in the Density wave propagation at the output instant with different reference Knudsen numbers.

Table 5
CPU time and memory cost in the density wave propagation problem at $t = 1$.

	CPU time (s)		Memory (kB)	
	AUGKS	UGKS	AUGKS	UGKS
Kn=0.0001	117.39	18451.00	15976	282592
Kn=0.001	12560.71	18510.30	223678	280564
Kn=0.01	18407.97	18570.53	278590	281632
Kn=0.1	18024.64	18339.93	280992	282012

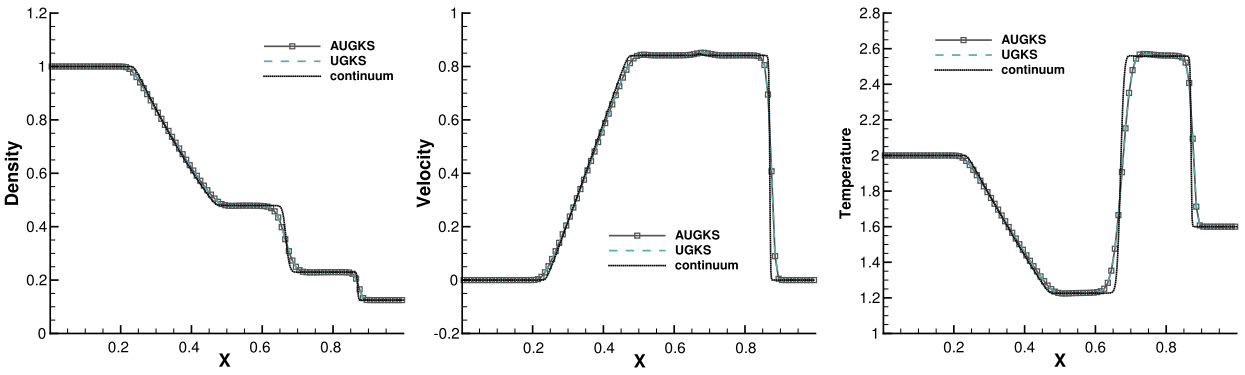

(a) Density (b) Velocity (c) Temperature

Fig. 9. Sod shock tube at $t = 0.2$ with reference Knudsen number $Kn = 0.0001$.

computational cost is proportional to the mesh points in the velocity space, it is expected that the computational efficiency is closely related to the size of non-equilibrium region. When the reference Knudsen number increases to $Kn = 0.001$, the CPU time and memory load of AUGKS increase correspondingly, while it is still more efficient than the original UGKS. As the rarefaction degree continues growing at $Kn = 0.01$ and 0.1, the discrete velocity space is used everywhere in the flow domain, and the computational cost in the AUGKS becomes equivalent as the original UGKS.

4.2. Sod shock tube

The next case is the Sod shock tube problem. The flow domain $x \in [0, 1]$ is divided into 100 uniform cells. The initial condition is set as

$$\rho = 1.0, U = 0.0, p = 1.0, \ x \leq 0.5,$$

$$\rho = 0.125, U = 0.0, p = 0.1, \ x > 0.5.$$

The simulations are performed with reference Knudsen numbers varying from $Kn = 0.0001$ to $Kn = 1.0$, corresponding to different flow regimes. The current criterion value for velocity space transformation is set as $B = 0.0001$. The velocity space is discretized into 80 uniform points for the update of particle distribution function. In the AUGKS and UGKS, the full Boltzmann collision operator is solved here by the fast spectral method [34]. The numerical solutions at $t = 0.2$ are presented in Fig. 9, 10, 11 and 12. The reference solution of continuum flow is calculated by the continuous GKS solver with 1000 cells, and the free molecular flow solution is derived from the collisionless Boltzmann equation.

In the simulation, the region with initial homogeneous spatial distribution of flow variables is calculated with a continuous velocity space, except at the central discontinuity the flow is simulated with a discretized velocity. As time evolves, the non-equilibrium region enlarges along with the use of discrete velocity space. As presented in Fig. 13a, at $Kn = 0.0001$ and $t = 0.2$, the flow domain is divided into some subzones, where the non-equilibrium particle distribution function inside rarefaction wave, contact discontinuity, and shock wave is fully resolved with the discretized velocity space, while in the rest near-equilibrium regions the Chapman-Enskog expansion is adopted over a continuous velocity space. The solutions of AUGKS at $Kn = 0.0001$ and $t = 0.2$ are presented in Fig. 9a, 9b, 9c, which match the benchmark continuum and UGKS solutions accurately. As the Knudsen number gets to $Kn = 0.001$ at $t = 0.2$, near-equilibrium region confines to a small part near the left tube boundary, where the distribution function has a continuous velocity space, which is shown in Fig. 13b. With increasing rarefaction effect, the distributions of flow variables deviate from the NS solutions gradually and tend to collisionless Boltzmann solutions. As the reference Knudsen number gets to $Kn = 0.01$, the Navier-Stokes solutions lose its validity quickly from the initial condition, and the non-equilibrium region occupies the whole tube at $t = 0.2$. The numerical solution approaches to the collisionless Boltzmann solution at $Kn = 1.0$, as shown in Fig. 11 and 12.

This test case illustrates the capacity of AUGKS to simulate flow in different regimes. The asymptotic preserving (AP) property is confirmed in the two limiting solutions. With increasing reference Knudsen number, there is a smooth transition

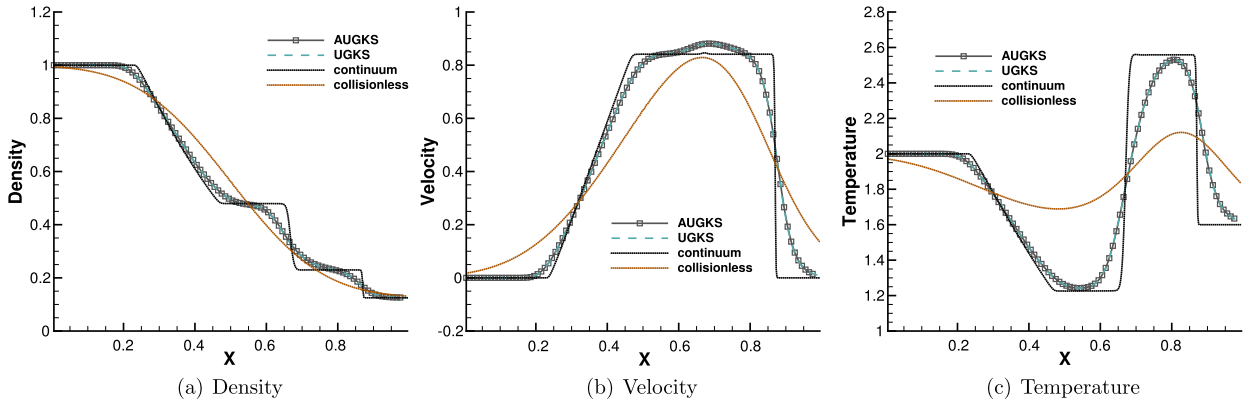

Fig. 10. Sod shock tube at $t = 0.2$ with reference Knudsen number $Kn = 0.001$.

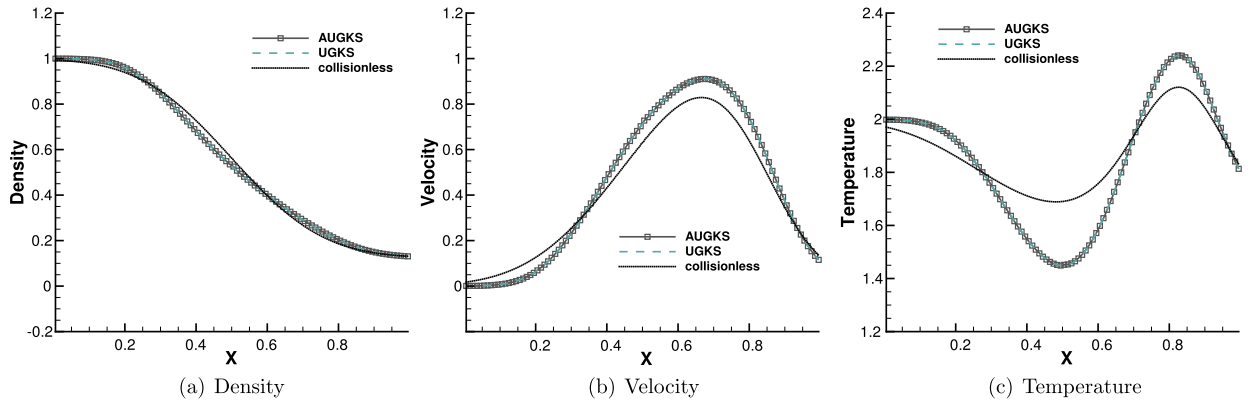

Fig. 11. Sod shock tube at $t = 0.2$ with reference Knudsen number $Kn = 0.01$.

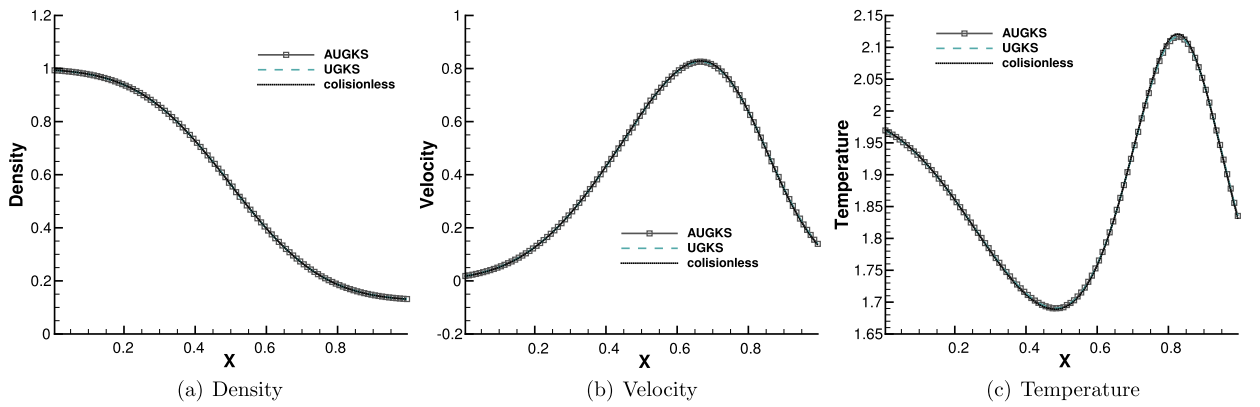

Fig. 12. Sod shock tube at $t = 0.2$ with reference Knudsen number $Kn = 1.0$.

from the Euler solution of the Riemann problem to collisionless Boltzmann solution. Table 6 presents the CPU time and memory cost at the output instant $t = 0.2$ from the current adaptive scheme and original UGKS method. As shown, the AUGKS is about 3.63 times faster than UGKS at $Kn = 0.0001$, and saves 48% memory load. When the degree of rarefaction increases, the CPU time of AUGKS increases correspondingly, while it is still more efficient than the original UGKS.

4.3. Rayleigh flow

A Rayleigh flow forms over a plate which suddenly acquires a constant parallel velocity and temperature. In this test case, we follow the setup by Sun [42]. As shown in Fig. 14, the argon gas is at rest and has a unit temperature initially. When $t > 0$, the plate suddenly moves with a constant velocity $U_w = 0.0296$ and temperature $T_w = 1.36$. The momentum and

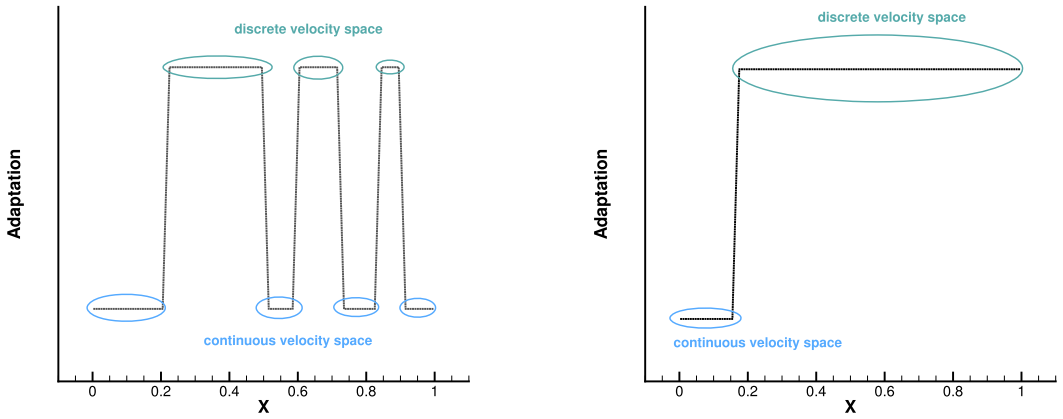

(a) $Kn = 0.0001$ (b) $Kn = 0.001$

Fig. 13. Velocity space adaptation inside the shock tube at $t = 0.2$.

Table 6
CPU time and memory cost in the Sod shock tube case at $t = 0.2$.

	CPU time (s)		Memory (kB)	
	AUGKS	UGKS	AUGKS	UGKS
Kn=0.0001	2042.98	7421.70	98960	190448
Kn=0.001	3537.73	7430.82	154988	188428
Kn=0.01	4692.52	7547.99	186860	188420
Kn=0.1	5694.46	7275.40	184836	188432

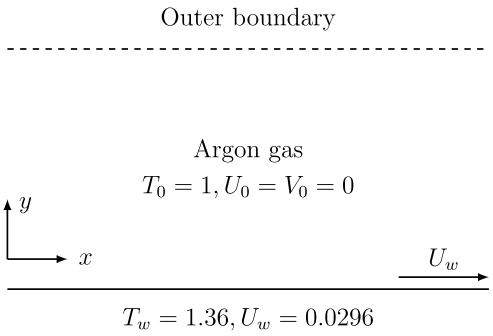

Fig. 14. Schematic of Rayleigh problem.

energy are transported into the flow field through a shearing effect in the unsteady process. A physical domain $y \in [0, 1]$ with 100 uniform cells are set up for the simulation, and the 32 uniform points are used in the velocity space, where the particle distribution function is updated directly. In this case, the full Boltzmann collision operator in the AUGKS and UGKS is calculated by the fast spectrum method [34]. The current switching criterion of velocity space is set as $B = 0.0001$.

Numerical simulations are performed with a series of reference Knudsen number, and solutions at same output times are plotted in Fig. 15, 16, 17 and 18. Besides AUGKS solutions, the UGKS and DSMC results with full Boltzmann collision operator are also provided as benchmarks. With Maxwell's fully accommodation boundary condition, Bird [4] proposed an analytical solution from the collisionless Boltzmann equation when the time is much less than the reference mean collision time $\tau_0 = \ell_0/v_0$, where ℓ_0 is particle mean free path and v_0 is the mean molecular speed. The analytical collisionless solution is also plotted in figures.

As presented in Fig. 15, 16, 17 and 18, for the case at $Kn = 2.66$ and $t = 0.1\tau_0$, the AUGKS recovers exact collisionless Boltzmann solution. In the transition regime $Kn = 0.266$ and $Kn = 0.0266$ at $t = \tau_0$ and $t = 10\tau_0$, the numerical solutions deviate from collisionless solutions gradually due to increasing intermolecular collisions. At $t = 100\tau_0$ and $Kn = 0.00266$ corresponding to a near-continuum regime, the current adaptive scheme recovers the Navier-Stokes solutions with intensive intermolecular collisions. As plotted, in all cases the AUGKS solutions agree well with the benchmark solutions from DSMC and UGKS. It is worth mentioning that in comparison with DSMC method, the current Boltzmann-equation-based adaptive unified scheme has no statistical scattering, which is beneficial in low speed simulations.

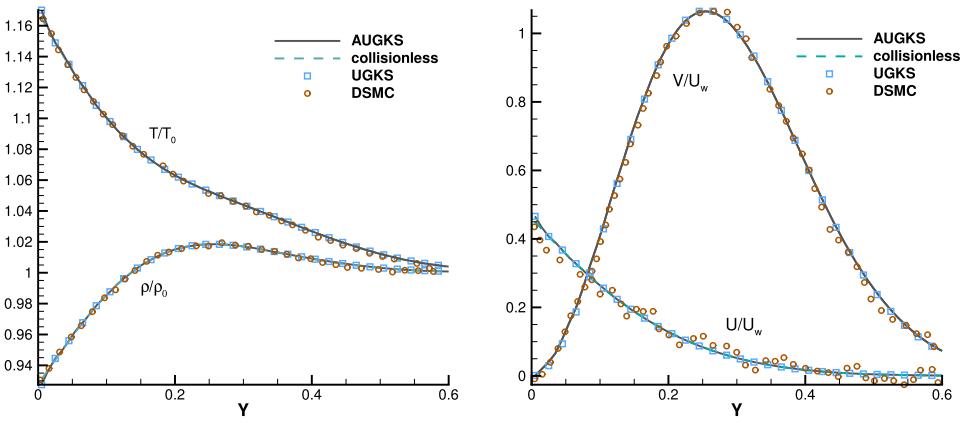

(a) Density and Temperature (b) Velocity

Fig. 15. Rayleigh flow at $t = 0.1\tau_0$ with reference Knudsen number $Kn = 2.66$.

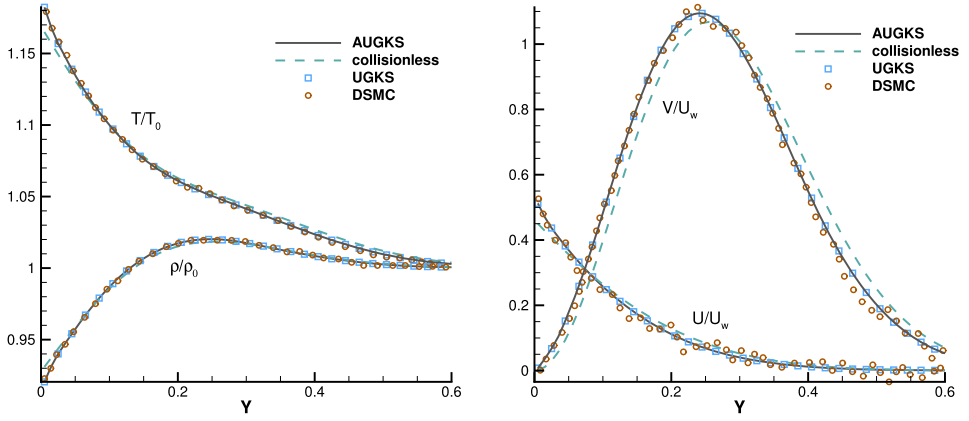

(a) Density and Temperature (b) Velocity

Fig. 16. Rayleigh flow at $t = \tau_0$ with reference Knudsen number $Kn = 0.266$.

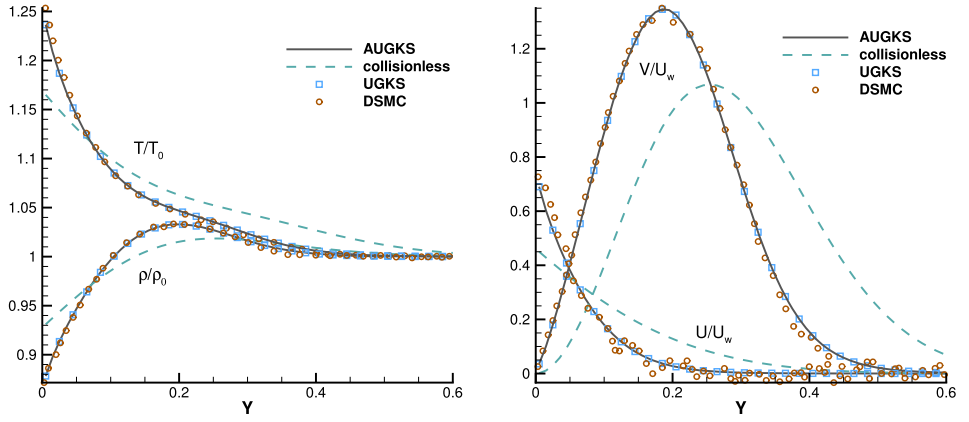

(a) Density and Temperature (b) Velocity

Fig. 17. Rayleigh flow at $t = 10\tau_0$ with reference Knudsen number $Kn = 0.0266$.

Fig. 19 presents the velocity space adaptation inside the flow domain at the output time. In the case with $Kn = 0.00266$, in the near-wall region with large slope of macroscopic variables, the AUGKS uses a discrete velocity space, while a continuous velocity space is used in the outer region. As the Knudsen number increases, the enhanced dimensionless viscosity and heat conductivity lead to a large non-equilibrium region. As a result, the non-equilibrium region enlarges faster. For

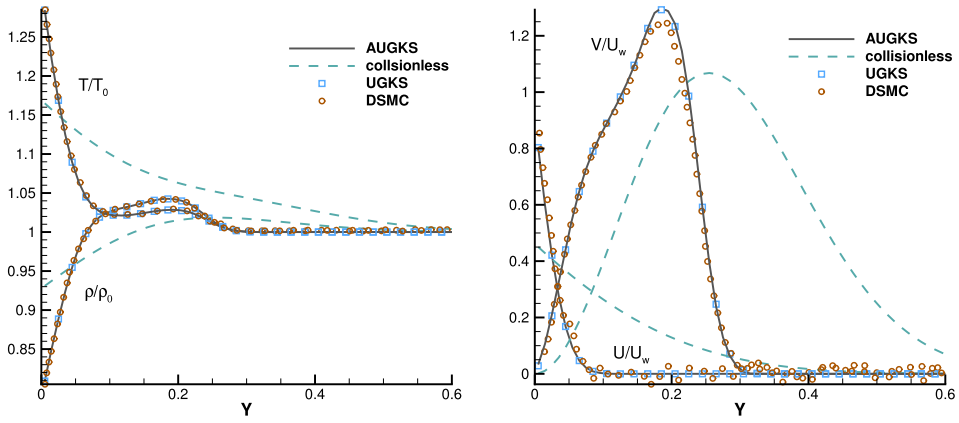

(a) Density and Temperature (b) Velocity

Fig. 18. Rayleigh flow at $t = 100\tau_0$ with reference Knudsen number $Kn = 0.00266$.

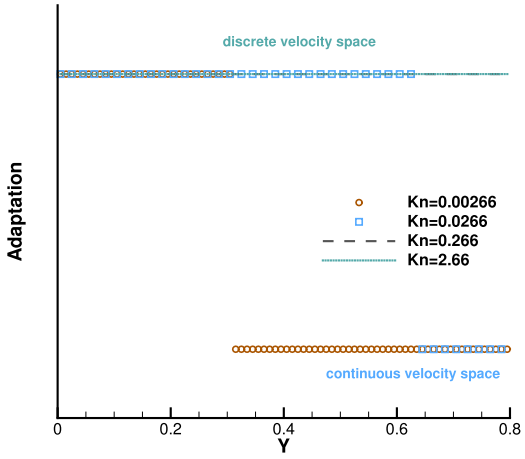

Fig. 19. Velocity space adaptation in the Rayleigh flow at the output instant with different reference Knudsen numbers.

Table 7
CPU time and memory cost in the Rayleigh problem.

	CPU time (s)		Memory (kB)	
	AUGKS	UGKS	AUGKS	UGKS
Kn=0.00266	1003.59	7477.10	184937	543232
Kn=0.0266	2223.62	7460.21	358828	539140
Kn=0.266	3751.75	7438.06	544128	540796
Kn=2.66	4637.19	7457.87	537760	543828

the case $Kn = 0.266$, in all flow region the distribution function deviates from the Chapman-Enskog solution and its evolution must be followed with a discretized velocity space. Table 7 presents the computational cost of the AUGKS and UGKS. When $Kn = 0.00266$, the AUGKS is 7.45 times faster than the original UGKS, with a 66% memory reduction. When the Knudsen number increases, the enhanced non-equilibrium regions increase the computational cost of AUGKS. From the current numerical experiments, it is clear that the AUGKS provides a self-adjusted algorithm from continuum to rarefied flow simulation with the consideration of both accuracy and efficiency.

4.4. Nozzle flow

The nozzle flow connecting different flow regimes is an ideal case to test the capacity of AUGKS in capturing multiple scale flow dynamics. The schematic of the nozzle problem is presented in Fig. 20. The argon gas is enclosed in a rectangular box $x \in [0, 2.2]$, $y \in [-0.5, 0.5]$. The velocity space is discretized into 28×28 uniform points for the update of particle distribution function. The switching criterion of velocity space in this case is set as $B = 0.0005$. In this case, the collision

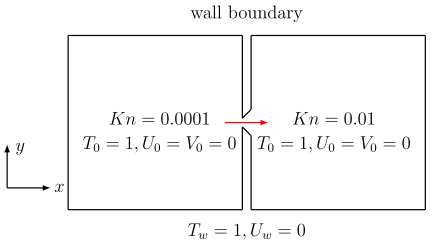

Fig. 20. Schematic of Nozzle jet problem.

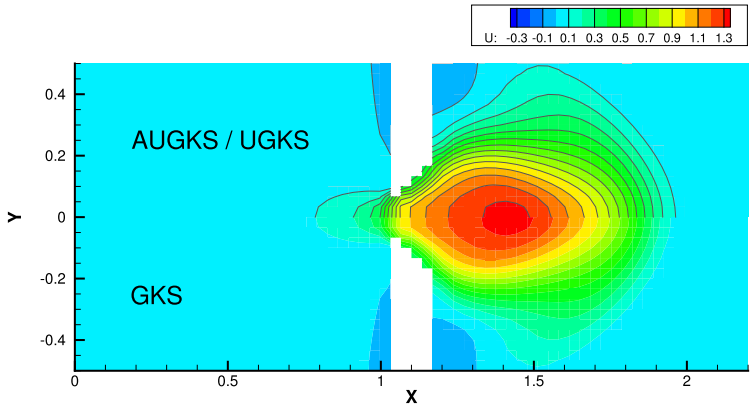

(a) U-velocity

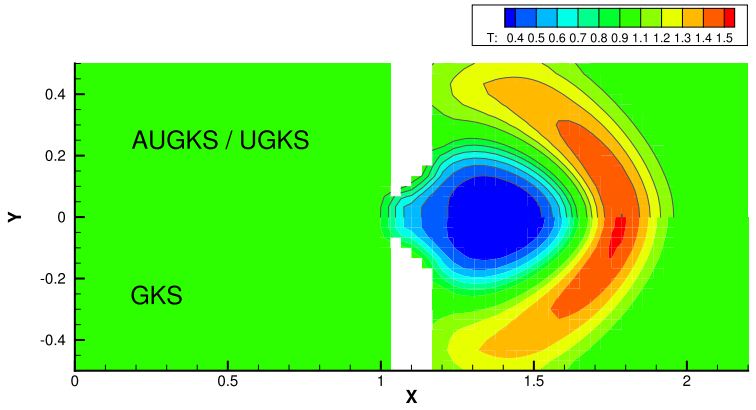

(b) Temperature

Fig. 21. Density and Temperature contours at $t = 5\tau_0$ (upper flood: AUGKS, upper lines: UGKS, lower: GKS).

term in AUGKS and UGKS is the Shakhov model. The computational domain is divided into two parts which are connected through a nozzle. The gas density in the left is 100 times higher than that in the right part, and the initial Knudsen numbers are $Kn_L = 0.0001$ and $Kn_R = 0.01$ respectively. The initial gas is at rest and has the same temperature inside two subdomains, same as the cavity wall. The Maxwell's diffusive boundary condition is used at all walls. The nozzle entrance has a variable cross section from $\Delta y_L = 0.13$ to $\Delta y_R = 0.33$ along a length $\Delta x = 0.14$, from which a jet flow will be formed. The simulation is performed till $t = 50\tau_0$, where $\tau_0 = \ell_0/v_0$ is the mean collision time of initial argon gas in the right domain.

Fig. 21 and 22 present the solution contours of $U-$velocity and temperature at two times $t = 5\tau_0$ and $t = 20\tau_0$. The upper part of color contours are the results calculated by the AUGKS (flood) and UGKS (lines), while the lower part is the Navier-Stokes solutions provided by the GKS only with a continuous velocity space. As shown in the figures, the bow shock and expansion cooling region behind shock are captured by all methods. However, it is clear that at $Kn = 0.01$, the Navier-Stokes equations lose validity to quantitatively describe the flow evolution in the right domain, and it is necessary to use kinetic method to get accurate solutions here. Fig. 23 and 24 present the solutions along the horizontal center line of the box at times $t = 5\tau_0$ and $t = 20\tau_0$. It is clear that the AUGKS provides equivalent solutions as the NS ones in the

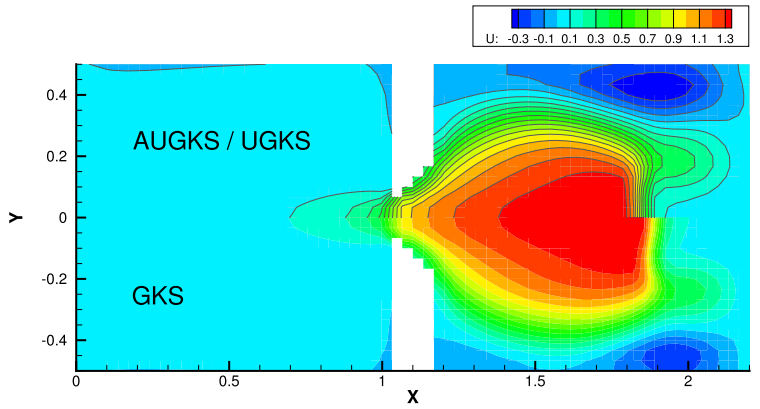

(a) U-velocity

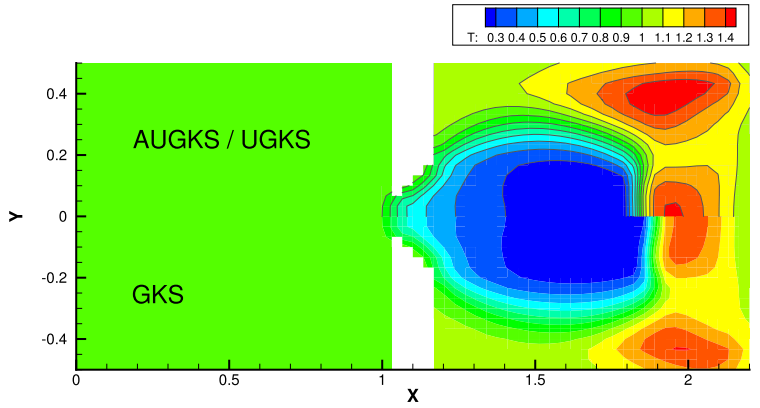

(b) Temperature

Fig. 22. Density and Temperature contours at $t = 20\tau_0$ (upper flood: AUGKS, upper lines: UGKS, lower: GKS).

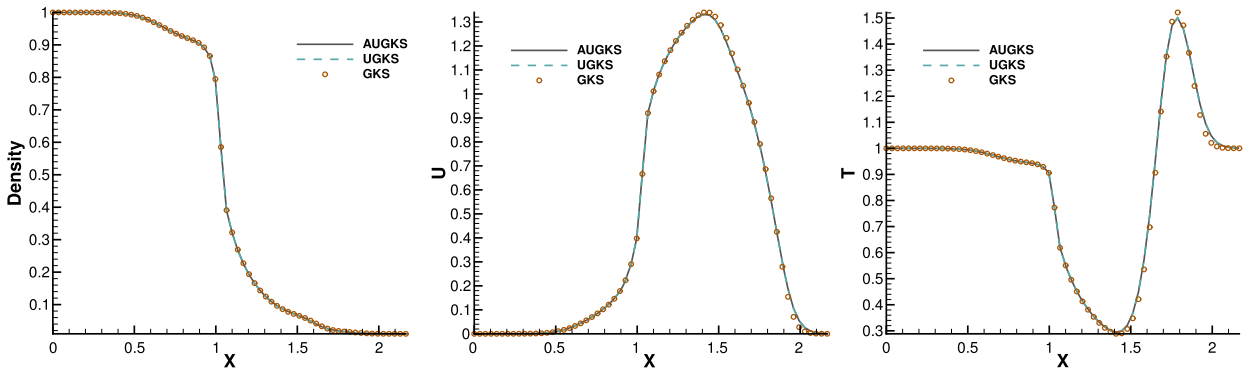

(a) Density (b) U-velocity (c) Temperature

Fig. 23. Solutions along the horizontal central line at $t = 5\tau_0$.

near-equilibrium left region, and with the Boltzmann solutions in the non-equilibrium right region. This test demonstrates the multiscale capability of the adaptive method to get the physical solutions in the corresponding flow regimes.

Fig. 25, 26 and 27 present the components of spatial slope a used in the velocity space switching criterion, the mean collision time, and the corresponding velocity space adaptation of the flow domain at three times $t = \tau_0,\ 5\tau_0,\ 20\tau_0$. As shown in the figures, the shock and expansion waves are the major sources for large flow gradients inside the domain. Accompanying with the high-density jet into the right domain, the mean collision time decreases in the jet region. With time increasing, the local flow structure becomes more complicated, leading to a large non-equilibrium region. As a result, the Chapman-Enskog expansion fails in the places where the strong non-equilibrium effects appear, and the discretized velocity space has to be used in AUGKS. Table 8 presents the computational cost of AUGKS, UGKS and GKS in this case.

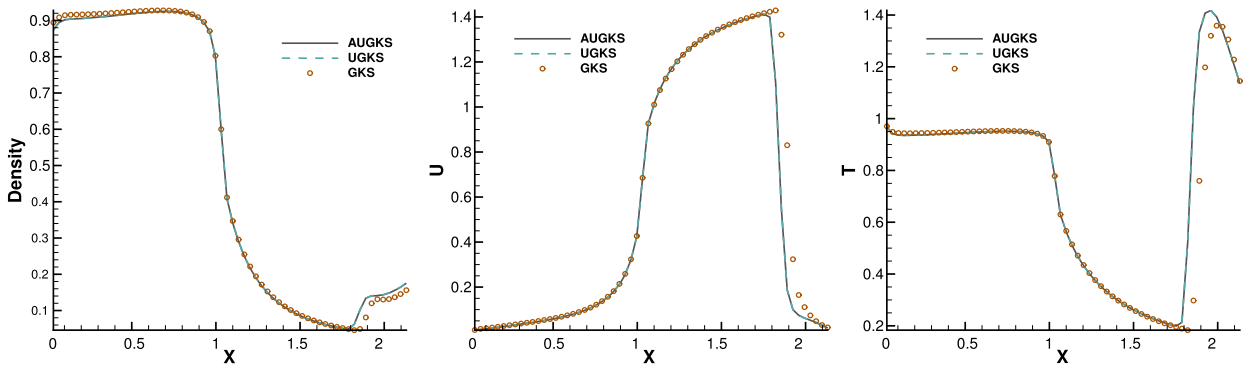

(a) Density (b) U-velocity (c) Temperature

Fig. 24. Solutions along the horizontal central line at $t = 20\tau_0$.

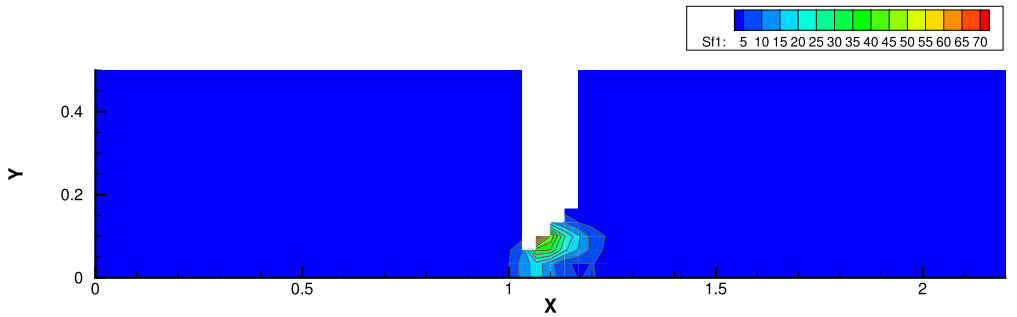

(a) a_1

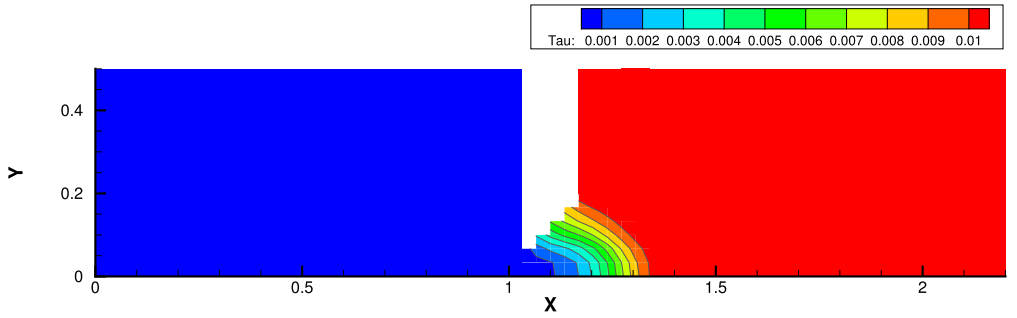

(b) Colliison time

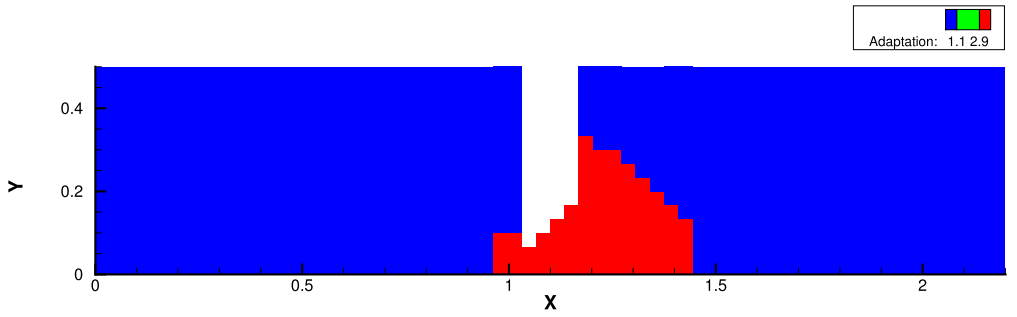

(c) Velocity adaptation

Fig. 25. Velocity space adaptation in the nozzle flow at $t = \tau_0$.

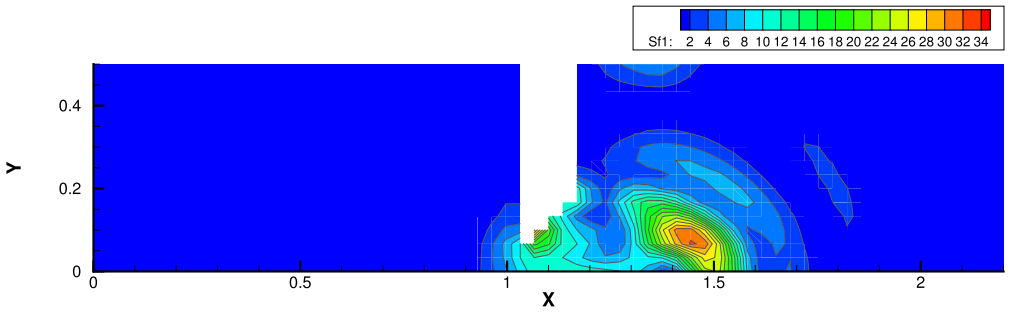

(a) a_1

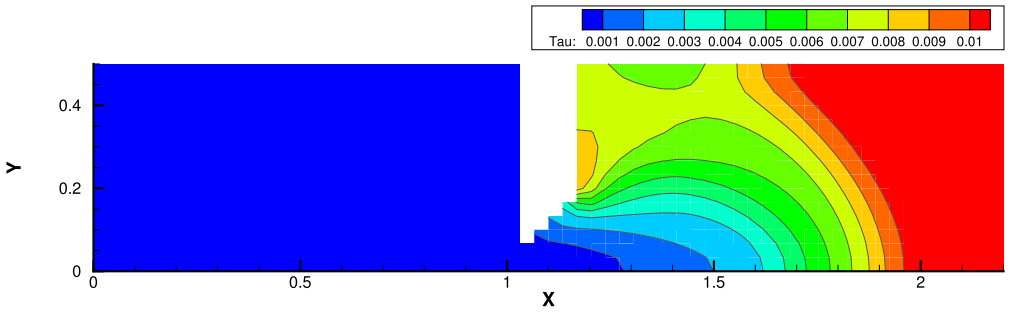

(b) Colliison time

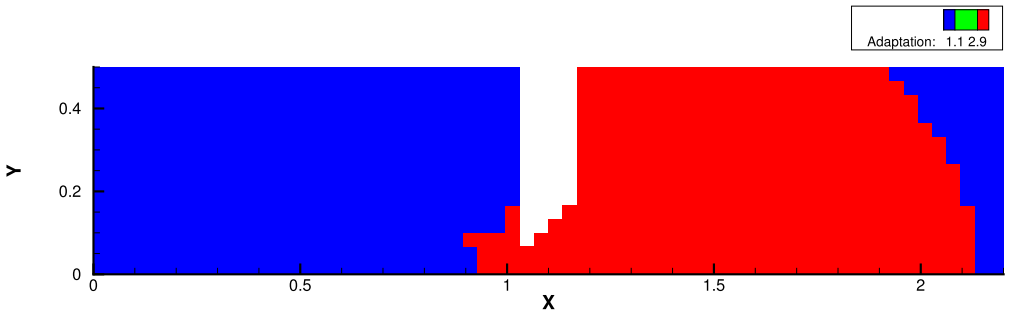

(c) Velocity adaptation

Fig. 26. Velocity space adaptation in the nozzle flow at $t = 5\tau_0$.

Table 8
CPU time and memory cost in the nozzle flow.

	AUGKS	UGKS	GKS
CPU time (s)	526.25	898.69	35.25
Memory (kB) ($t = 0$)	3614	74828	2636
Memory (kB) ($t = 50\tau_0$)	35125	74836	2640

With the current setup of physical mesh and velocity space, the continuous GKS solver is about 25 times faster than UGKS with discretized velocity space. The AUGKS is 1.7 times faster than the original UGKS. At the initial stage in the simulation, the memory cost in the AUGKS is on the same order as the GKS, which is about 1/30 of the UGKS. As flow evolves, the number of cells associated with discretized velocity space increases, and the corresponding memory cost gets higher. At the final time $t = 50\tau_0$, there are about 429 out of 914 total cells using continuous velocity space, and the corresponding memory size is 53% of the original UGKS.

4.5. Flow around circular cylinder

In the previous studies, the AUGKS in the simulation of unsteady flows is well validated. In this case, the flow passing through a circular cylinder is used to test the performance of current adaptive scheme for steady flow. The incoming gas

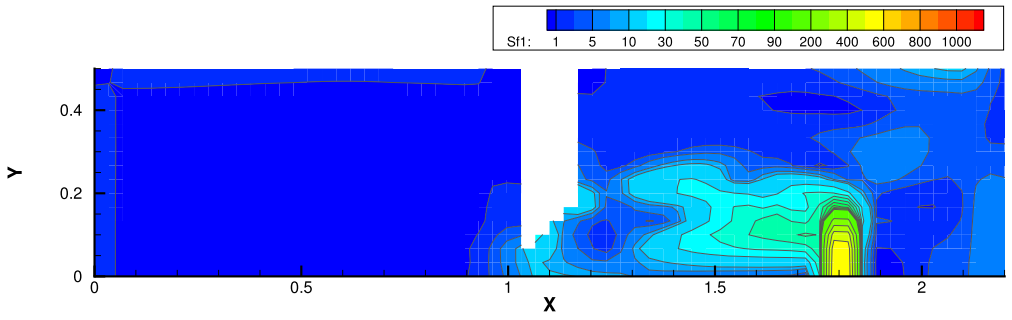

(a) a_1

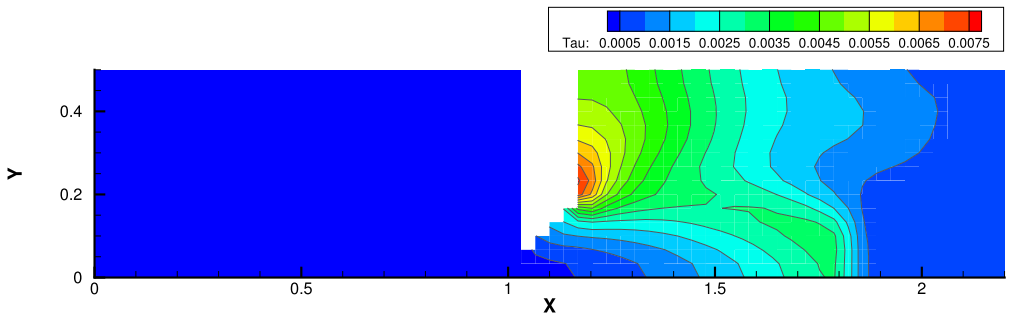

(b) Colliison time

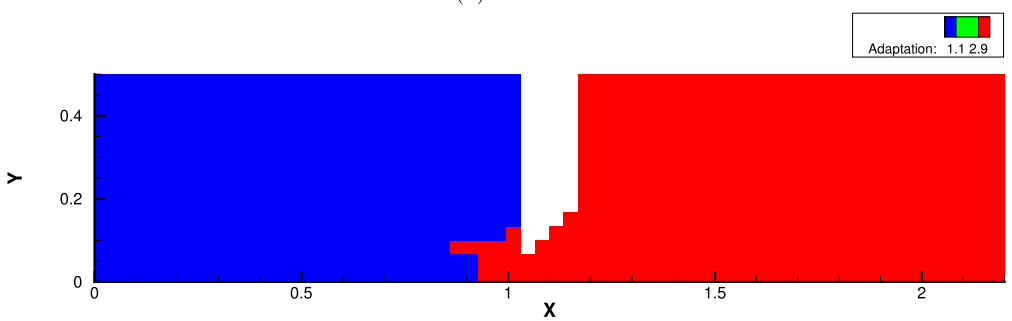

(c) Velocity adaptation

Fig. 27. Velocity space adaptation in the nozzle flow at $t = 20\tau_0$.

has a uniform velocity with Mach number $Ma = 5$ and the same temperature, such as $T = 273$ K, as the cylinder surface. The reference Knudsen number is set up as $Kn = 0.001$ and $Kn = 0.01$ relative to cylinder radius, and the corresponding dynamic viscosity is $\mu_{ref} = 7.313 \times 10^{-4}$ and $\mu_{ref} = 7.313 \times 10^{-3}$. In the calculation, 60 cells in radial direction and 100 cells in circumferential direction are used in physical domain. The velocity space is discretized into 41×41 velocity points for the update of particle distribution function. In this case, the collision term for particle distribution function in AUGKS and UGKS is modeled as the Shakhov model. The Maxwell's diffusive boundary condition is used at the surface of the cylinder. The switching criterion of particle velocity space is set as $B = 0.0005$.

For steady problem, the computational time can be further reduced with the help of the GKS with a continuous velocity space. A convergent coarse flow field can be first obtained by the GKS, and then used as the initial state in the subsequent adaptive method. The method for the computation of steady flow is the following.

1. From initial setup, use the GKS solver in the entire domain and obtain a convergent flow field.
2. Use the calculated macroscopic flow variables as the initial flow condition to get the particle distribution function with the discretized Chapman-Enskog form by Eq. (37).
3. Adapt the velocity space based on the current switching criterion in Eq. (42).
4. Use continuous velocity space in near-equilibrium flow region and discretized velocity space in non-equilibrium one, and continue the velocity adaptation with iterations until a convergent flow field is obtained.

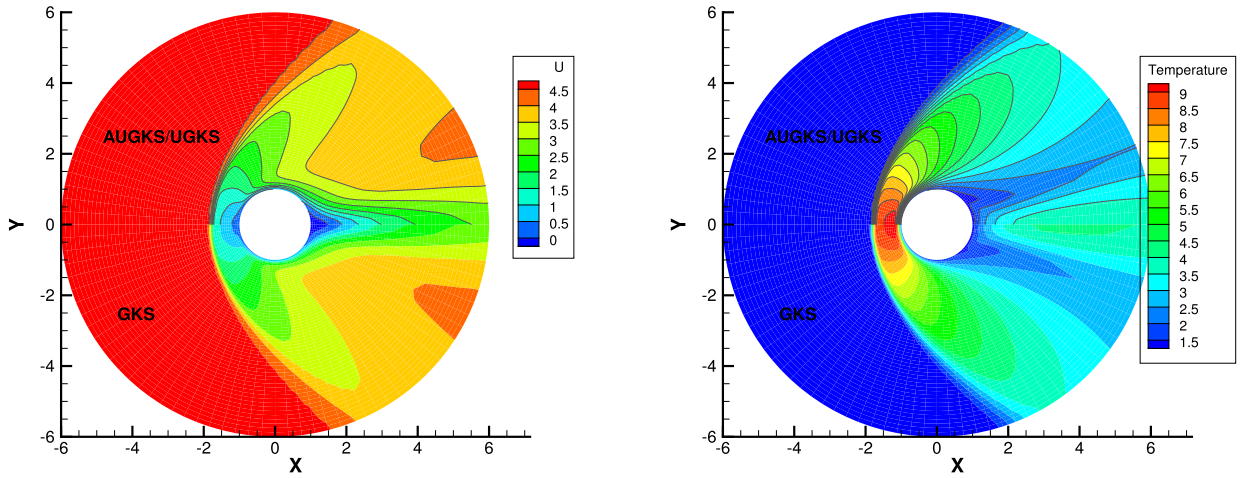

(a) U-velocity (b) Temperature

Fig. 28. Density and Temperature contours in the flow passing through cylinder at $Kn = 0.001$ (upper flood: AUGKS, upper lines: UGKS, lower flood: GKS).

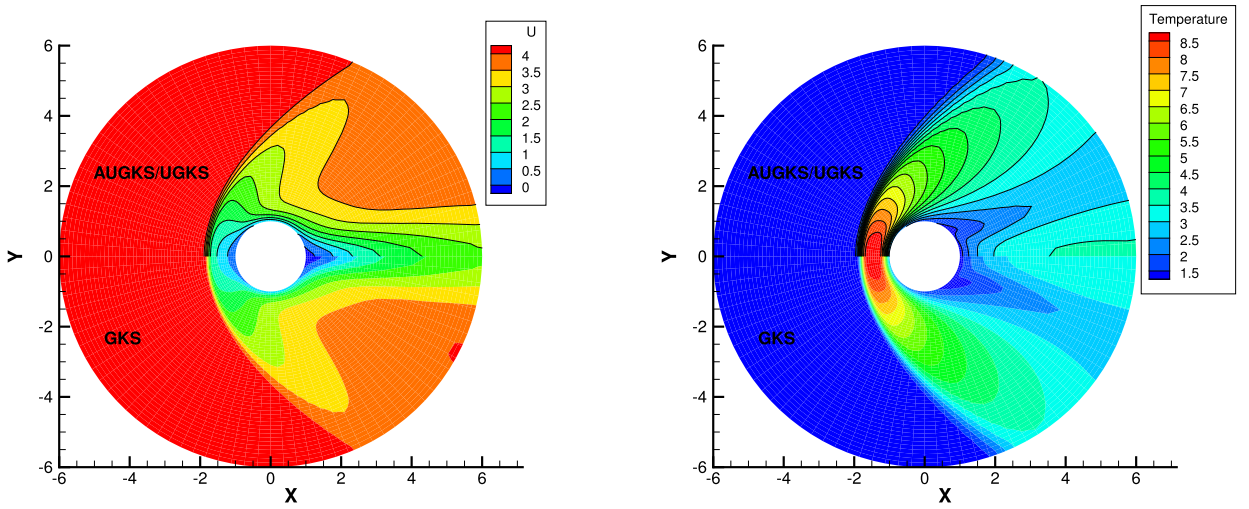

(a) U-velocity (b) Temperature

Fig. 29. Density and Temperature contours in the flow passing through cylinder at $Kn = 0.01$ (upper flood: AUGKS, upper lines: UGKS, lower flood: GKS).

Fig. 28 and Fig. 29 present the solution contours of $U-$velocity and temperature calculated by the AUGKS, UGKS and GKS methods respectively around the cylinder. The upper part of contours is the results of AUGKS (flood) and UGKS (solid line) solutions, and the lower part is the GKS solutions. As shown, the bow shock and expansion cooling region behind shock are well captured by all methods.

Fig. 30, 31, 32, 33 present the solutions along the horizontal center line in front of and behind the cylinder. At $Kn = 0.001$, the cell size and time step in the computation are much larger than particle mean free path and collision time. Due to the limited time-space resolution, all three methods become shock-capturing schemes, and a sharp shock profile is obtained in front of the cylinder in Fig. 30. Near the cylinder wall, due to the non-equilibrium gas dynamics in gas-surface interaction, there is a slight difference in the solutions provided by UGKS and GKS. At the same time, the gas density reduces a lot in the wake region behind cylinder with emerging rarefied regions, and there is a significant difference between UGKS and GKS solutions in Fig. 31.

When the reference Knudsen number gets to $Kn = 0.01$, a large particle mean free path leads to a wide shock structure. This non-equilibrium evolution is provided in the scale-dependent interface solution used in AUGKS and UGKS. However, the Chapman-Enskog expansion can only provide incomplete information about this process in continuous GKS solver. As a result, the GKS presents a narrower shock profile than that in AUGKS and UGKS in Fig. 32. In the wake region, due to the enlarged particle collision time at $Kn = 0.01$, the results provided by GKS differ significantly from AUGKS and UGKS solutions. The GKS with a continuous velocity space fails to predict physical solutions in these regions, and particle distribution function is updated explicitly in the AUGKS with a discretized particle velocity space. It is clear that the current velocity

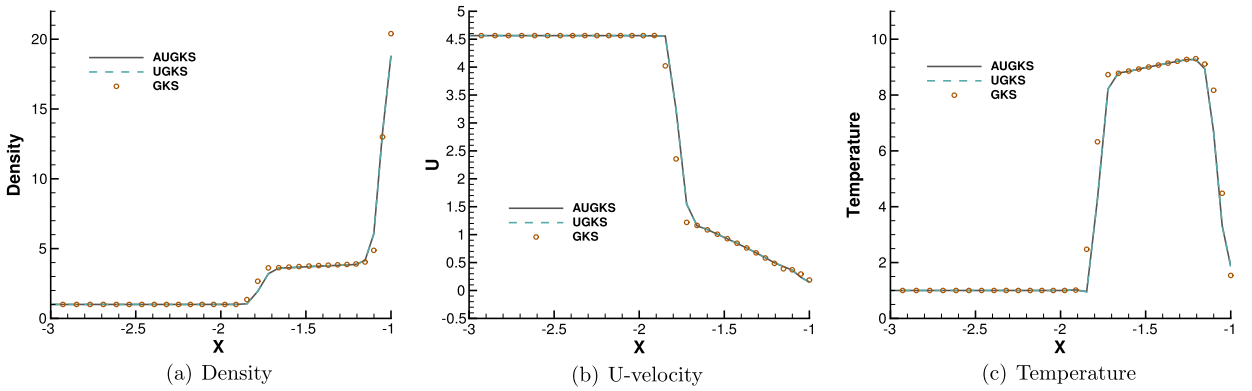

(a) Density (b) U-velocity (c) Temperature

Fig. 30. Solutions along the horizontal central line in front of cylinder at $Kn = 0.001$.

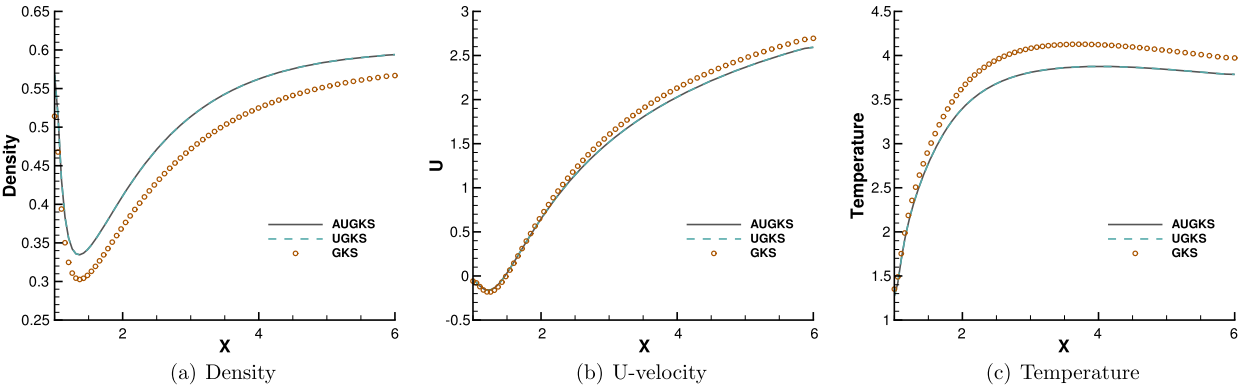

(a) Density (b) U-velocity (c) Temperature

Fig. 31. Solutions along the horizontal central line behind cylinder at $Kn = 0.001$.

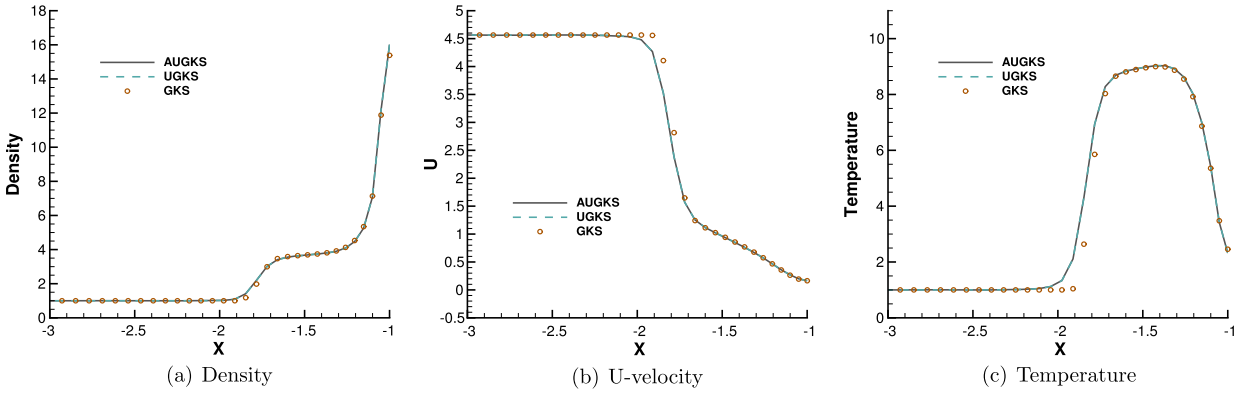

(a) Density (b) U-velocity (c) Temperature

Fig. 32. Solutions along the horizontal central line in front of cylinder at $Kn = 0.01$.

adaptive unified scheme captures the physical solutions as the NS in the near-equilibrium region and the UGKS ones in the non-equilibrium region.

Fig. 34 and 35 present two components of spatial slope **a** used in the velocity-space switching criterion, the mean collision time, and the adaptation of velocity space. As can be seen, the shock wave and boundary are two sources for high gradients of flow variables, leading to the failure of Chapman-Enskog expansion and Navier-Stokes solutions. Behind the cylinder, the low density wake leads to an increased particle collision time, which is shown in Fig. 34c and Fig. 35c. Therefore, a velocity adaptation is determined as shown in Fig. 34d and Fig. 35d. The incoming flow as well as a small region between the bow shock and cylinder is computed with continuous velocity space, while the rest non-equilibrium region are simulated by the UGKS with discrete velocity space. Due to an increased particle collision time, the non-equilibrium region with discrete particle velocity space is enlarged at $Kn = 0.01$ than that at $Kn = 0.001$.

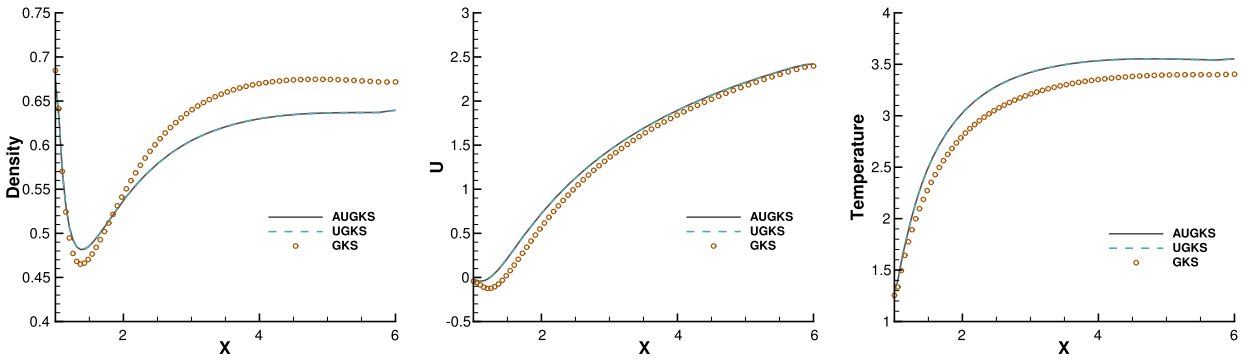

(a) Density (b) U-velocity (c) Temperature

Fig. 33. Solutions along the horizontal central line behind cylinder at $Kn = 0.01$.

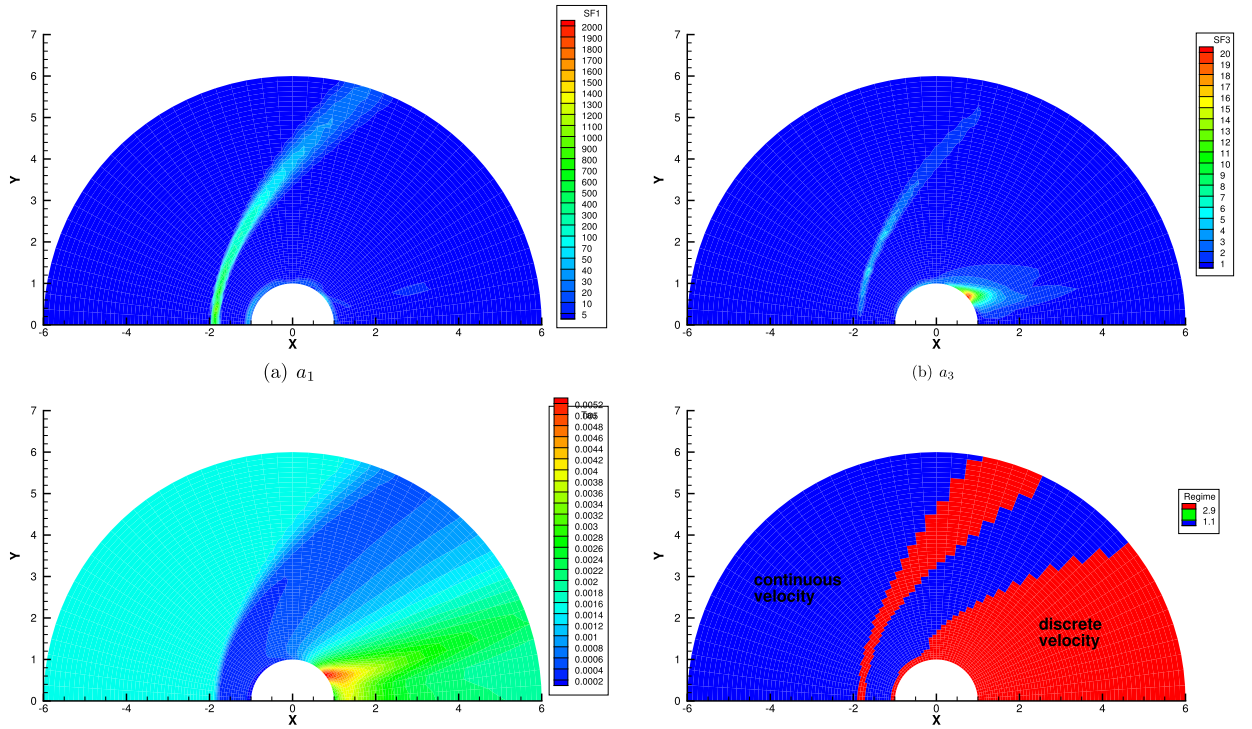

(a) a_1 (b) a_3

(c) Collision time (d) Velocity adaptation

Fig. 34. Velocity space adaptation in the flow domain at $Kn = 0.001$.

Table 9
CPU time and memory cost in the flow around circular cylinder.

	CPU time (s)			Memory (kB)		
	AUGKS	UGKS	GKS	AUGKS	UGKS	GKS
Kn=0.001	36130.68	117371.67	2975.07	452508	857520	14652
Kn=0.01	22145.10	75510.33	2536.55	614542	856944	12636

Table 9 presents the computational cost of AUGKS, UGKS and GKS at $Kn = 0.001$ and $Kn = 0.01$ respectively. With the current setup of physical mesh and velocity space, the continuous GKS solver is about 30 times faster than the UGKS, and the AUGKS is about 3.3 times faster than the original UGKS in this steady flow problem. In the convergent steady state, there are about 3196 cells at $Kn = 0.001$ and 1992 cells at $Kn = 0.01$ out of 6000 total cells using continuous velocity space, and the corresponding memory size is about 47% and 67% of that in the original UGKS.

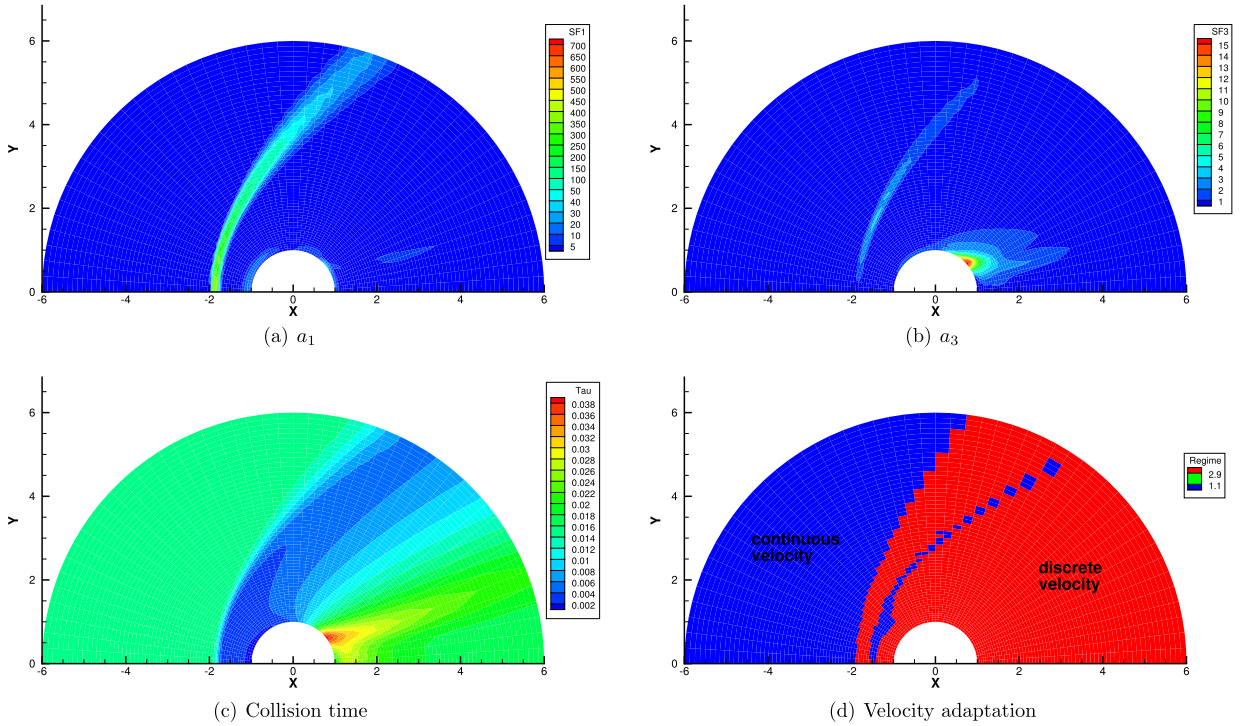

(a) a_1 (b) a_3

(c) Collision time (d) Velocity adaptation

Fig. 35. Velocity space adaptation in the flow domain at $Kn = 0.01$.

5. Conclusion

The gas dynamics has intrinsically multiple scale nature due to the large variations of density and characteristic length scale of the flow structures. Based on scale-dependent time evolution solution of the Boltzmann model equation, a velocity-space adaptive unified gas kinetic scheme has been developed in this paper for the simulation of multiscale flow transport. The current adaptive algorithm is based on a dynamic velocity-space transformation, where the particle velocity space is continuous in the near-equilibrium region and discrete in the non-equilibrium one. A switching criterion for particle velocity space transformation is proposed based on the Chapman-Enskog expansion and is validated through numerical experiments. Under a unified framework with the adaptation of particle velocity space only, the AUGKS needs no buffer zone for the connection of continuum and kinetic solutions. This compact property leads to an effective method for multiscale flow simulation with unsteadiness and complex geometries. Compared with discrete-velocity-space framework of the original UGKS, the AUGKS is more efficient and less memory demanding for multiscale flow computations. The AUGKS provides a useful tool for non-equilibrium flow studies, and it can be further improved in the future with the combination of implicit and multigrid techniques [43,44].

Declaration of competing interest

The authors declare that they have no known competing financial interests or personal relationships that could have appeared to influence the work reported in this paper.

Acknowledgement

The authors would like to thank Dr. Lei Wu for the help on numerical implementation of the fast spectral method for the Boltzmann collision term. The current research is supported by Hong Kong research grant council (16206617), and National Science Foundation of China (11772281, 91852114).

Appendix A. Nomenclature

Here a nomenclature used in AUGKS is provided in defining the constants, variables, and functions (Table 10).

Table 10
The nomenclature of adaptive unified gas kinetic scheme.

Variables	
f	particle distribution function
$\mathbf{u}$	particle velocity
$Q(f,f)$	Boltzmann collision operator
$S(f)$	Shakhov relaxation operator
$Q(f)$	General collision operator
f^+	Shakhov equilibrium distribution function
$\mathbf{W}$	Macroscopic conservative variables
ρ	Density
$\mathbf{U}$	Macroscopic flow velocity
T	Temperature
$\mathbf{c}$	Particle peculiar velocity
λ	Characteristic quantity with $\lambda = \rho/(2p)$
Pr	Prandtl number
Kn	Knudsen number
ψ	Vector of collision invariants
τ	Collision time
$\mathbf{F}$	Flux of macroscopic conservative variables
ξ	Internal degrees of freedom for reduced distribution function
f_0	Initial particle distribution function at the beginning of n-th time step
σ	Slope of initial distribution function along x direction
θ	Slope of initial distribution function along y direction
$\bar{a}^{L,R}$	Leftward/Rightward slopes of equilibrium distribution function along x direction
$\bar{b}$	Slope of equilibrium distribution function along y direction
$\bar{A}$	Time derivative of equilibrium distribution function
$H[x]$	Heaviside step function
$a^{l,r}$	Leftward/Rightward slopes of distribution function along x direction in Chapman-Enskog expansion
$b^{l,r}$	Leftward/Rightward slopes of distribution function along y direction in Chapman-Enskog expansion
$A^{l,r}$	Leftward/Rightward time derivatives of distribution function in Chapman-Enskog expansion
a	Slope of distribution function along x direction in Chapman-Enskog expansion in continuous case
b	Slope of distribution function along y direction in Chapman-Enskog expansion in continuous case
A	Time derivative of distribution function in Chapman-Enskog expansion in continuous case
B	Switching criterion for velocity space transformation

References

[1] Sydney Chapman, Thomas George Cowling, The Mathematical Theory of Non-uniform Gases: An Account of the Kinetic Theory of Viscosity, Thermal Conduction and Diffusion in Gases, Cambridge University Press, 1970.
[2] Hsue-Shen Tsien, Superaerodynamics, mechanics of rarefied gases, J. Aeronaut. Sci. 13 (12) (1946) 653–664.
[3] Vasiliĭ Aristov, Direct methods for solving the Boltzmann equation and study of nonequilibrium flows.
[4] Graeme Austin Bird, Molecular Gas Dynamics and the Direct Simulation of Gas Flows, 1994.
[5] V.I. Kolobov, R.R. Arslanbekov, V.V. Aristov, A.A. Frolova, Sergey A. Zabelok, Unified solver for rarefied and continuum flows with adaptive mesh and algorithm refinement, J. Comput. Phys. 223 (2) (2007) 589–608.
[6] V.I. Kolobov, R.R. Arslanbekov, Towards adaptive kinetic-fluid simulations of weakly ionized plasmas, J. Comput. Phys. 231 (3) (2012) 839–869.
[7] Francis Filbet, Thomas Rey, A hierarchy of hybrid numerical methods for multiscale kinetic equations, SIAM J. Sci. Comput. 37 (3) (2015) A1218–A1247.
[8] Jean-François Bourgat, Patrick Le Tallec, Moulay Tidriri, Coupling Boltzmann and Navier–Stokes equations by friction, J. Comput. Phys. 127 (2) (1996) 227–245.
[9] Sudarshan Tiwari, Axel Klar, An adaptive domain decomposition procedure for Boltzmann and Euler equations, J. Comput. Appl. Math. 90 (2) (1998) 223–237.
[10] S. Tiwari, Coupling of the Boltzmann and Euler equations with automatic domain decomposition, J. Comput. Phys. 144 (2) (1998) 710–726.
[11] Iain D. Boyd, Timothy R. Deschenes, Hybrid particle-continuum numerical methods for aerospace applications, Technical report, Dept. of Aerospace Engineering, Michigan Univ., Ann Arbor, 2011.
[12] Jonathan M. Burt, Iain D. Boyd, A hybrid particle approach for continuum and rarefied flow simulation, J. Comput. Phys. 228 (2) (2009) 460–475.
[13] H.S. Wijesinghe, R.D. Hornung, A.L. Garcia, N.G. Hadjiconstantinou, et al., Three-dimensional hybrid continuum-atomistic simulations for multiscale hydrodynamics, J. Fluids Eng. 126 (5) (2004) 768–777.
[14] Thomas E. Schwartzentruber, Leonardo C. Scalabrin, Iain D. Boyd, A modular particle–continuum numerical method for hypersonic non-equilibrium gas flows, J. Comput. Phys. 225 (1) (2007) 1159–1174.
[15] Giacomo Dimarco, Lorenzo Pareschi, Hybrid multiscale methods II. Kinetic equations, Multiscale Model. Simul. 6 (4) (2008) 1169–1197.
[16] Giacomo Dimarco, Raphaël Loubère, Vittorio Rispoli, A multiscale fast semi-Lagrangian method for rarefied gas dynamics, J. Comput. Phys. 291 (2015) 99–119.
[17] Nicolas Crouseilles, Giacomo Dimarco, Mohammed Lemou, Asymptotic preserving and time diminishing schemes for rarefied gas dynamic, Kinet. Relat. Models 10 (2017) 643–668.
[18] Pierre Degond, Jian-Guo Liu, Luc Mieussens, Macroscopic fluid models with localized kinetic upscaling effects, Multiscale Model. Simul. 5 (3) (2006) 940–979.
[19] Pierre Degond, Giacomo Dimarco, Luc Mieussens, A moving interface method for dynamic kinetic–fluid coupling, J. Comput. Phys. 227 (2) (2007) 1176–1208.
[20] Roberto Roveda, David B. Goldstein, Philip L. Varghese, Hybrid Euler/particle approach for continuum/rarefied flows, J. Spacecr. Rockets 35 (3) (1998) 258–265.
[21] Roberto Roveda, David B. Goldstein, Philip L. Varghese, Hybrid Euler/direct simulation Monte Carlo calculation of unsteady slit flow, J. Spacecr. Rockets 37 (6) (2000) 753–760.

[22] C. David Levermore, William J. Morokoff, B.T. Nadiga, Moment realizability and the validity of the Navier–Stokes equations for rarefied gas dynamics, Phys. Fluids 10 (12) (1998) 3214–3226.
[23] Tao Xiong, Jing-Mei Qiu, A hierarchical uniformly high order dg-imex scheme for the 1D BGK equation, J. Comput. Phys. 336 (2017) 164–191.
[24] Carlo Cercignani, The Boltzmann Equation and Its Applications, Springer, 1988.
[25] Kun Xu, Direct Modeling for Computational Fluid Dynamics: Construction and Application of Unified Gas-Kinetic Schemes, World Scientific, 2015.
[26] Kun Xu, Juan-Chen Huang, A unified gas-kinetic scheme for continuum and rarefied flows, J. Comput. Phys. 229 (20) (2010) 7747–7764.
[27] Chang Liu, Kun Xu, Quanhua Sun, Qingdong Cai, A unified gas-kinetic scheme for continuum and rarefied flows IV: full Boltzmann and model equations, J. Comput. Phys. 314 (2016) 305–340.
[28] Tianbai Xiao, Qingdong Cai, Kun Xu, A well-balanced unified gas-kinetic scheme for multiscale flow transport under gravitational field, J. Comput. Phys. 332 (2017) 475–491.
[29] Tianbai Xiao, Kun Xu, Qingdong Cai, Tiezheng Qian, An investigation of non-equilibrium heat transport in a gas system under external force field, Int. J. Heat Mass Transf. 126 (2018) 362–379.
[30] Shi Jin, Asymptotic preserving (ap) schemes for multiscale kinetic and hyperbolic equations: a review, in: Lecture Notes for Summer School on Methods and Models of Kinetic Theory (M&MKT), Porto Ercole, Grosseto, Italy, 2010, pp. 177–216.
[31] Kun Xu, A gas-kinetic bgk scheme for the Navier–Stokes equations and its connection with artificial dissipation and Godunov method, J. Comput. Phys. 171 (1) (2001) 289–335.
[32] E.M. Shakhov, Generalization of the Krook kinetic relaxation equation, Fluid Dyn. 3 (5) (1968) 95–96.
[33] Clément Mouhot, Lorenzo Pareschi, Fast algorithms for computing the Boltzmann collision operator, Math. Comput. 75 (256) (2006) 1833–1852.
[34] Lei Wu, Craig White, Thomas J. Scanlon, Jason M. Reese, Yonghao Zhang, Deterministic numerical solutions of the Boltzmann equation using the fast spectral method, J. Comput. Phys. 250 (2013) 27–52.
[35] Lei Wu, Jason M. Reese, Yonghao Zhang, Solving the Boltzmann equation deterministically by the fast spectral method: application to gas microflows, J. Fluid Mech. 746 (2014) 53–84.
[36] Francis Filbet, Shi Jin, A class of asymptotic-preserving schemes for kinetic equations and related problems with stiff sources, J. Comput. Phys. 229 (20) (2010) 7625–7648.
[37] Pierre-Louis Lions, et al., Compactness in Boltzmann's equation via Fourier integral operators and applications. I, J. Math. Kyoto Univ. 34 (2) (1994) 391–427.
[38] Taku Ohwada, Kun Xu, The kinetic scheme for the full-Burnett equations, J. Comput. Phys. 201 (1) (2004) 315–332.
[39] Kun Xu, Chang Liu, A paradigm for modeling and computation of gas dynamics, Phys. Fluids 29 (2) (2017) 026101.
[40] Iain D. Boyd, Gang Chen, Graham V. Candler, Predicting failure of the continuum fluid equations in transitional hypersonic flows, Phys. Fluids 7 (1) (1995) 210–219.
[41] Alejandro L. Garcia, Berni J. Alder, Generation of the Chapman–Enskog distribution, J. Comput. Phys. 140 (1) (1998) 66–70.
[42] Quanhua Sun, Information Preservation Methods for Modeling Micro-Scale Gas Flows, 2003.
[43] Yajun Zhu, Chengwen Zhong, Kun Xu, Implicit unified gas-kinetic scheme for steady state solutions in all flow regimes, J. Comput. Phys. 315 (2016) 16–38.
[44] Yajun Zhu, Chengwen Zhong, Kun Xu, Unified gas-kinetic scheme with multigrid convergence for rarefied flow study, Phys. Fluids 29 (9) (2017) 096102.